

RESEARCH ARTICLE

10.1002/2015JA021051

Key Points:

- Sector boundary can act as an obstacle to the propagation of SEPs
- Background solar wind is an important factor in the variation of shock strength
- At least 50% of the variance in SEP flux can be explained by the shock Mach number

Correspondence to:

C.-C. Wu,
chin-chun.wu@nrl.navy.mil

Citation:

Wu, C.-C., K. Liou, A. Vourlidas, S. Plunkett, M. Dryer, S. T. Wu, and R. A. Mewaldt (2016), Global magnetohydrodynamic simulation of the 15 March 2013 coronal mass ejection event—Interpretation of the 30–80 MeV proton flux, *J. Geophys. Res. Space Physics*, 121, 56–76, doi:10.1002/2015JA021051.

Received 27 JAN 2015

Accepted 16 NOV 2015

Accepted article online 18 NOV 2015

Published online 23 JAN 2016

Global magnetohydrodynamic simulation of the 15 March 2013 coronal mass ejection event—Interpretation of the 30–80 MeV proton flux

Chin-Chun Wu¹, Kan Liou², Angelos Vourlidas², Simon Plunkett¹, Murray Dryer³, S. T. Wu⁴, and Richard A. Mewaldt⁵
¹Naval Research Laboratory, Washington, District of Columbia, USA, ²Applied Physics Laboratory, The Johns Hopkins University, Laurel, Maryland, USA, ³Space Weather Predictions Center, Emeritus, NOAA, Boulder, Colorado, USA, ⁴CSPAR, University of Alabama, Huntsville, Alabama, USA, ⁵California Institute of Technology, Pasadena, California, USA

Abstract The coronal mass ejection (CME) event on 15 March 2013 is one of the few solar events in Cycle 24 that produced a large solar energetic particle (SEP) event and severe geomagnetic activity. Observations of SEP from the ACE spacecraft show a complex time-intensity SEP profile that is not easily understood with current empirical SEP models. In this study, we employ a global three-dimensional (3-D) magnetohydrodynamic (MHD) simulation to help interpret the observations. The simulation is based on the H3DMHD code and incorporates extrapolations of photospheric magnetic field as the inner boundary condition at a solar radial distance (r) of 2.5 solar radii. A Gaussian-shaped velocity pulse is imposed at the inner boundary as a proxy for the complex physical conditions that initiated the CME. It is found that the time-intensity profile of the high-energy (>10 MeV) SEPs can be explained by the evolution of the CME-driven shock and its interaction with the heliospheric current sheet and the nonuniform solar wind. We also demonstrate in more detail that the simulated fast-mode shock Mach number at the magnetically connected shock location is well correlated ($r_{cc} \geq 0.7$) with the concurrent 30–80 MeV proton flux. A better correlation occurs when the 30–80 MeV proton flux is scaled by $r^{-1.4}$ ($r_{cc} = 0.87$). When scaled by $r^{-2.8}$, the correlation for 10–30 MeV proton flux improves significantly from $r_{cc} = 0.12$ to $r_{cc} = 0.73$, with 1 h delay. The present study suggests that (1) sector boundary can act as an obstacle to the propagation of SEPs; (2) the background solar wind is an important factor in the variation of IP shock strength and thus plays an important role in manipulation of SEP flux; (3) at least 50% of the variance in SEP flux can be explained by the fast-mode shock Mach number. This study demonstrates that global MHD simulation, despite the limitation implied by its physics-based ideal fluid continuum assumption, can be a viable tool for SEP data analysis.

1. Introduction

Interplanetary coronal mass ejections (ICMEs) are one of the two major solar wind structures that have been connected with solar energy particle (SEP) events in the heliosphere [e.g., Reames, 1999]. There is a substantial amount of observational evidence to indicate that CME-driven shocks are the source for the “gradual” SEPs [e.g., Kahler *et al.*, 1986, 1987]. For example, there is a close association between SEP events and slow drifting Type II radio bursts generated by shocks near the Sun [Wild *et al.*, 1963] and a linear correlation between the logarithmic of proton peak intensity and the logarithmic of speed of their associated CME [Kahler, 2001]. As another empirical association, the SEP peak flux is correlated better with the CME speed than with the X-ray flare peak flux [Gopalswamy *et al.*, 2003].

When observed at a remote site, the time-intensity profile of SEP events is manifested not only by changes in the source of the SEPs but also by transport of the SEPs, thus complicating the study of SEPs. Observations of SEP events are usually made using a single or two spacecraft orbiting around the Sun (for example, ACE, Wind, and STEREO-A/B). Properties of CME-driven shocks (SEP sources) may undergo substantial changes while propagating outward from the Sun. Because of limited spacecraft coverage, shock surface regions of a given Mach number intensity are only observationally available in a fragmentary form [e.g., Berdichevsky *et al.*, 2009]. In addition, SEPs are charged particles and are magnetically confined. Therefore, the intensity profile of SEP is controlled by the magnetic field structure and polarity. Moreover, then, the solar sector boundaries may block SEPs from reaching the observers, thus

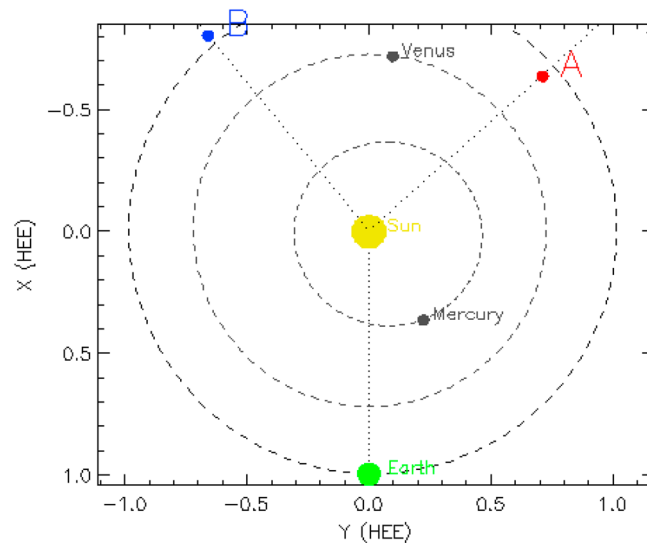


Figure 1. The locations of the STEREO-A and STEREO-B spacecraft are identified by red and blue dots, respectively. The locations of the Sun and the Earth are identified by yellow and green dots, respectively. The ACE (and Wind) spacecraft is located near the Earth, along the Sun-Earth line.

of concurrent fast-mode shocks. A further study of the events also showed that there is a good linear relationship between the logarithmic time-intensity profile of helium (^4He) SEPs ($E > \sim 10 \text{ MeV n}^{-1}$) and the concurrent fast-mode shock Mach number [Liou *et al.*, 2013].

The simulation conducted by Liou *et al.* [2012, 2013] was 1.5-D, thus ignoring the geometry of the magnetic field by which energetic charged particles are gyroconfined and followed. In this study, we will apply a 3-D simulation code to include the magnetic field structure to study the relationship between the intensity of SEPs and fast shock strength (Mach number).

In the following sections, we will first describe the general solar wind conditions (section 2.1) and the SEP event (section 2.2) associated with the 15 March 2013 CME. In section 3, we will describe the global simulation model followed by the simulation results and comparisons with SEP flux in section 4. Discussion and conclusions will be given in sections 5 and 6, respectively.

2. Observations

2.1. CME on 15 March 2013

On 15 March 2013, NOAA reported a long duration M1.1 X-ray flare at 05:46 UT from active region (AR) 11692 at N11E12. The flare reached a peak value at 06:58 UT and ended at 08:35 UT. EUV 193 Å observations from the Atmospheric Imaging Assembly [Lemen *et al.* [2012]] instrument on board the Solar Dynamics Observatory [Pesnell *et al.* [2012]] spacecraft showed expanding loops beginning at ~06:03 UT. A Type IV source was detected at 06:20 UT in the metric range by the Learmonth radio spectrograph. The Wind/WAVES instrument detected an intermittent type II source from 07:00 to about 21:30 UT associated with the expanding CME's shock.

The CME was well observed by the imagers aboard the STEREO and SOHO spacecraft. Figure 1 shows the positions of the three spacecraft around the heliosphere on 15 March 2013. The positions of STEREO-A (W132), STEREO-B (E141), the Sun, and the Earth are marked in red, blue, yellow, and green dots, respectively. The ACE spacecraft was located at the L-1 in the Sun-Earth line. The Earth was located at 7.2°S on 15 March. The CME was first seen in C2 (SOHO/LASCO) at 07:12 UT as a bright loop with leading edge at $\sim 3.8 R_S$. The CME expanded into the C3 field of view (FOV) at ~07:30 UT and left the FOV by 11:18 UT as a symmetric halo. The average CME speed through both C2 and C3 fields was $\sim 980 \text{ km/s}$. The STEREO COR2-A and COR2-B showed an expanding asymmetric halo CME during 06:54–09:24 UT. The estimated CME speed was $\sim 1000 \text{ km/s}$ (<http://umbra.nascom.nasa.gov/lasco/observations/halo/2013/130315/>). In Figure 2, we show

reducing the SEP flux. As a consequence, direct comparisons of SEP characteristics with shock properties to test acceleration theories are difficult, if not impossible, with current observational techniques.

On the other hand, numerical simulation may provide a reasonable means for resolving the limitation of shock observations. Recently, Liou *et al.* [2012] used one-dimensional, (actually 1.5-D), time-dependent, magneto-hydrodynamic (MHD) simulations to simulate shocks driven by two large CME events that occurred during the Halloween epoch (28–31 October 2003). They showed that there is a good linear relationship between the logarithmic flux of oxygen SEPs ($E > \sim 10 \text{ MeV n}^{-1}$) observed by the ACE spacecraft and the Mach numbers



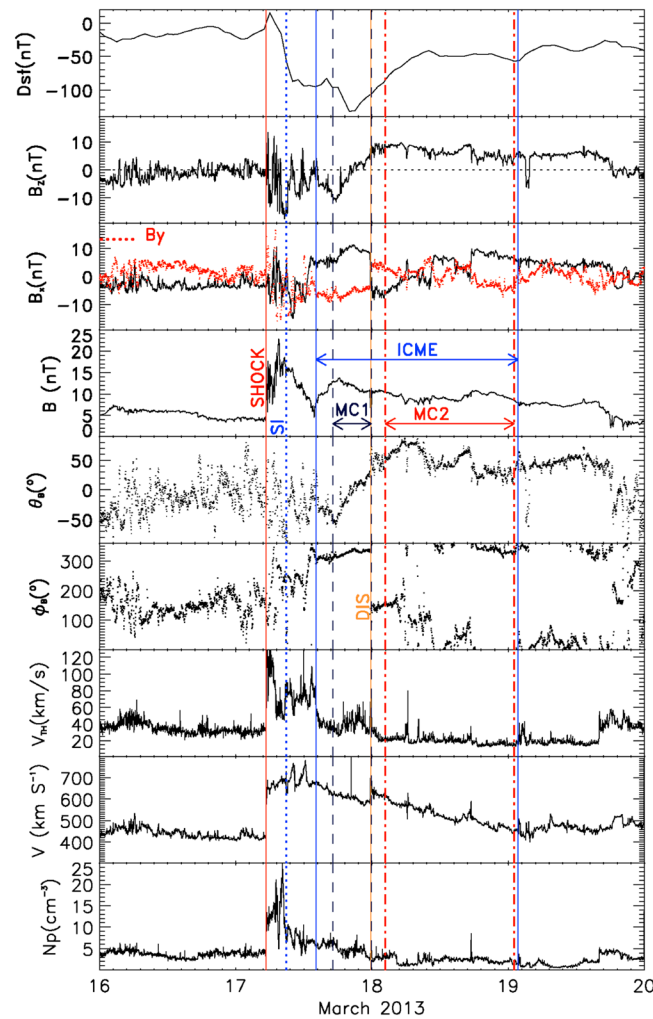


Figure 3. Geomagnetic activity, Dst , and in situ measurements of solar wind parameters from Wind spacecraft and derived parameters during 16–19 March 2013. (first–ninth panels) Proton density, velocity, thermal speed, ϕ_B , θ_B , IMF B_{total} (B), B_x , B_y (red dots), and B_z , respectively. The ICME is bounded by two vertical blue solid lines. The two MCs are bounded by two vertical black dashed lines (MC1), and orange dash-dotted line (MC2), respectively. Vertical red solid and orange solid lines indicate the IP shock and a discontinuity arrival time at Wind. Blue dotted line indicates the location of a stream interface, “SI.”

stop times are 17:07:33 on 17 March and 23:52:21 on 17 March for MC1, and 2:22:37 on 17 March and 1:52:31 on 18 March for MC2 (R. P. Lepping, private communication, 2015). The sizes (radii) of these two MCs are 0.071 AU for MC1 and 0.20 AU for MC2. Note that a MC is defined as a region in the solar wind having enhanced magnetic field strength, a smooth change in field direction as observed by a spacecraft passing through the MC and low proton plasma beta compared to the ambient proton temperature [Burlaga *et al.*, 1981].

Orientation of IMF θ_B (Figure 3, fifth panel) rotated smoothly from -60° at the MCL’s front boundary to $+80^\circ$ at the MCL’s rear boundary. The IMF B_z was -10 and 8 nT at the MCL’s front and rear boundaries, respectively. The value of Dst dropped further to -132 nT during the passage of the MCL’s front boundary through the Earth. During the IMF southward turning, a discontinuity (marked as a vertical orange dotted line, “DIS”) appeared in the middle of the MCL. At the same time IMF ϕ_B rotated almost 180° (Figure 3, sixth panel): B_z was near constant in the region between the DIS and the MCL’s rear boundary, direction of B_x changed from positive to negative (black curves in Figure 3, third panel), and the direction of B_y changed from negative to positive (red dotted curves in Figure 3, third panel).

(Figures 2, middle, and 2, bottom). Its larger extent along the eastern FOV of COR2-A suggests that the flux rope is oriented along a SE–NW axis. A 3-D reconstruction of the shock would be needed (e.g., forward modeling [Wood *et al.*, 2012]) for fully describing the shock geometry.

2.2. In Situ Solar Wind and Solar Energetic Particle Events

Figure 3 shows in situ solar wind observations (and derived parameters) from the Wind spacecraft, which was located at the L1 Lagrangian point, and the geomagnetic activity index, Dst (top panel). An IP shock arrived at the Wind spacecraft at ~ 05 UT on 17 March 2013. Dst dropped to ~ -100 nT while the z component of the interplanetary magnetic field (IMF) was turning southward in the sheath region behind the shock. (The sheath is defined as the region between an IP shock and the front boundary of a magnetic cloud (MC), magnetic cloud-like (MCL) structure, or ICME.) A dip in the z component (in GSE coordinate system) of the IMF reached a value of -18 nT in the sheath. The duration of the sheath across the Wind spacecraft was ~ 9 h. Dst finally dropped to -132 nT at 20 UT on 17 March when the ICME moved past the Wind spacecraft. There were two MCs embedded in the ICME as indicated in Figure 3 by the two vertical dashed lines (MC1) and two dotted lines (MC2) within the two vertical solid lines (ICME). The two MCs are separated by a discontinuity (DIS). The start and

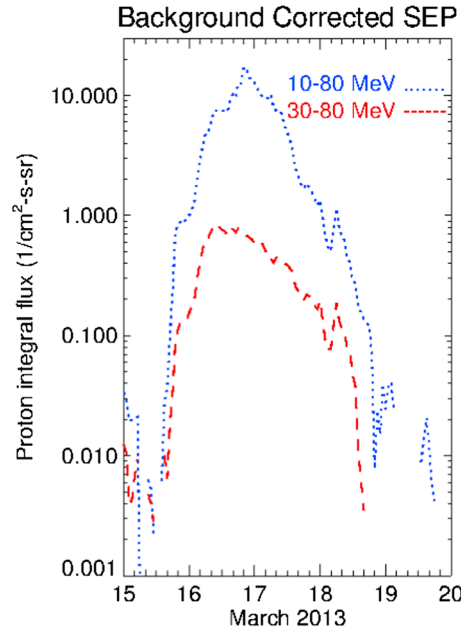


Figure 4. Intensity-time profile of solar energetic proton integral flux by the Solar Isotope Spectrometer (SIS) on board the Advanced Composition Explorer (ACE) spacecraft for two energy ranges: 10–30 MeV (blue dotted line) and 30–80 MeV (red dashed line) during the period 15–19 March 2013.

STEREO-B recorded an enhancement of SEP flux at ~08UT on 15 March which was ~1 h after the CME erupted but STEREO-A did not record any SEP flux enhancement (not shown), as expected from a classical undisturbed Parker spiral field. Figure 4 shows the time-intensity profile of proton SEPs recorded by the Solar Isotope Spectrometer (SIS) [Stone *et al.*, 1998] on board the ACE during the period of 15–19 March 2013. Blue and red curves represent SEP flux with energy > 10 MeV and > 30 MeV, respectively. Notice that ACE recorded two SEP flux enhancements: one at ~20UT on 15 March and the other at ~05 UT on 16 March, corresponding to ~12 and 22 h, respectively, after the CME was first seen by STEREO. We will use our H3DMHD model described in the following section to explain the two SEP enhancements, and two subsequent decreases, using our simulation result.

3. Global 3-D Simulation Model and Wave Tracing Method

3.1. Global 3-D Simulation Model

A global, time-dependent, numerical simulation model, WSA + HAFv.2 + 3DMHD model [e.g., Wu *et al.*, 2007a, 2007b] is used to investigate the evolution of CMEs from the Sun (at $18 R_S$) to the Earth environment and beyond (~1.6 AU). The system is driven by a time series of photo-

spheric magnetic maps composed from daily solar photospheric magnetograms (<http://wso.stanford.edu>). The WSA (Wang-Sheeley-Arge) model uses the observed line-of-sight magnetic field at the photosphere extrapolated to $2.5 R_S$ [e.g., Wang and Sheeley, 1990; Arge and Pizzo, 2000]. Use of these data to provide solar wind velocity and radial interplanetary magnetic fields (IMFs) at $2.5 R_S$ is described by Arge and Pizzo [2000]. The HAF (Hakamada-Akasofu-Fry) model is a physics-based kinematic model that takes inputs from WSA and propagates to $18 R_S$ [Fry *et al.*, 2001, and references therein]. A fully 3-D, time-dependent MHD simulation code [Han, 1977; Han *et al.*, 1988; Detman *et al.*, 1991, 2006] takes output from the HAF code and solves a set of ideal-MHD equations using an extension scheme of the two-step Lax-Wendroff finite difference methods [Lax and Wendroff, 1960]. Ideal MHD is used in the 3-D MHD model, which solves the basic conservation laws (mass, momentum, and energy) as shown in equations (1)–(3) with the induction equation (equation (4)) to take into account the nonlinear interaction between plasma flow and magnetic field.

$$\frac{D\rho}{Dt} + \rho \nabla \cdot \mathbf{V} = 0 \quad (1)$$

$$\rho \frac{D\mathbf{V}}{Dt} = -\nabla p + \frac{1}{\mu_0} (\nabla \times \mathbf{B}) \times \mathbf{B} - \rho \frac{GM_S(r)}{r^2} \mathbf{r} \quad (2)$$

$$\frac{\partial}{\partial t} \left[\rho p + \frac{1}{2} \rho |\mathbf{V}|^2 + \frac{|\mathbf{B}|^2}{2\mu_0} \right] + \nabla \cdot \left[\mathbf{V} \left\{ \rho e + \frac{1}{2} \rho |\mathbf{V}|^2 + p \right\} + \frac{\mathbf{B} \times (\mathbf{V} \times \mathbf{B})}{\mu_0} \right] = -\mathbf{v} \cdot \rho \frac{GM_S(r)}{r^2} \mathbf{r} \quad (3)$$

$$\frac{\partial \mathbf{B}}{\partial t} = \nabla \times (\mathbf{V} \times \mathbf{B}) \quad (4)$$

where t , r , ρ , \mathbf{V} , \mathbf{B} , p , and e are time, radius, density, velocity, magnetic field, thermal pressure, and internal energy. The internal energy, $e \equiv p/[(\gamma - 1)\rho]$. Additional symbols γ , M_S , G are the polytropic index, the solar mass, and the gravitational constant. $\gamma = 5/3$ is used for this study since it is a better value than other values (e.g., $\gamma = 1.25$ or 1.45) to use for in situ solar wind data at 1 AU [e.g., Wu *et al.*, 2011; Liou *et al.*, 2014]. The MHD governing equations are cast in uniform, spherical grids. This model is capable of simulating “effects” of CMEs

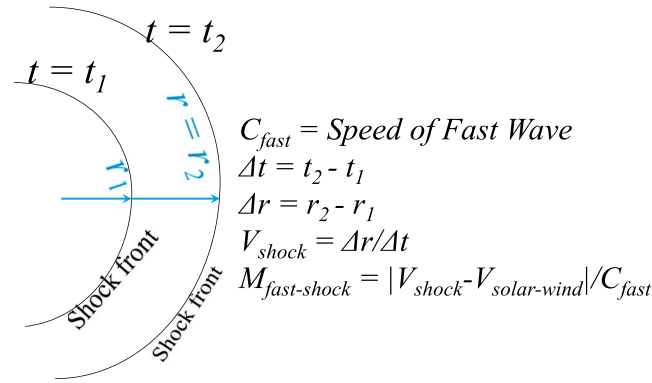


Figure 5. Schematic illustration for the wave tracing method (adapted from Figure 1 of Wu *et al.* [2012]). V_{shock} is the shock propagation speed, and $V_{solar-wind}$ is the upstream solar wind speed.

propagating in the solar wind. This general scheme has been well developed and successfully used in various conditions: cases for single CME events occurred on 12 May 1997 [Wu *et al.*, 2007a], 3 April 2010 [Wood *et al.*, 2011], and 1 August 2010 [Wu *et al.*, 2011]. Cases for multiple CME events (CME-CME interaction) occurred on 7 March 2011 [Wood *et al.*, 2012] and during the Halloween epoch 2003 [Wu *et al.*, 2007b, 2012]. An unusual case for an extremely fast CME (CME speed > 3000 km/s) on 23 July 2012 was discussed by Dryer *et al.* [2012].

To initiate the CME, a velocity pulse of Gaussian shape is imposed at the inner boundary of the computational domain ($r = 2.5 R_S$). The observed CME information such as the CME source location, onset time, and speed are used to construct the velocity pulse. The duration of the velocity pulse is the only free parameter to match the arrival time of the CME-driven shock and the CME profile at Earth.

3.2. Wave Tracing Method for Computing Shock Strength/Mach Number

The Wave Tracing Method (WTM) developed by Wu *et al.* [1996] is used to identify shock locations and to compute shock strength (e.g., the shock Mach number). WTM has been used in several previous studies for both one-dimensional simulation results [e.g., Wu *et al.*, 1996, 2004, 2006], and 3-D simulation results [e.g., Wu *et al.*, 2012; Dryer *et al.*, 2012; Liou *et al.*, 2014]. Figure 5 shows the schematic illustration of the concept of WTM for a fast shock. The procedure starts with manually determining the upstream location of the shock (r_i) using solar wind density, temperature, and speed and the total magnetic strength at a time step (t_i). To make sure it is the shock upstream, we visually inspect the solar wind plasma and field parameters immediately following the predetermined point to see if they satisfy the fast-mode shock conditions. The same procedure is applied to the time series of data radially outward along fixed polar and azimuthal angles. The shock speed $V_{shock}(i)$ at r_i in the inertial frame fixed to the Sun is calculated as $V_{shock}(i) = (r_{i+1} - r_i) / (t_{i+1} - t_i)$. This procedure is repeated for all time steps until all shock locations are identified for all radial directions. We then compute the shock normal, n , for each of every shock location using analytical geometry. We calculate the wave speed ($C_{Alfvén}$, C_{fast} , or C_{slow}) using plasma and field data at a grid point next to the shock location in the preshock region (upstream of the shock). Then we calculate the shock strength (Mach number) defined as $M_{fast} = V^* / C_{fast}$. V^* is the bulk velocity in a frame of reference, where $V^* = V_{solar-wind} - V_{shock}$ ($V_{solar-wind}$ is solar wind speed.) $C_{fast}^2 = \frac{1}{2} [C_{sound}^2 + V_{Alfvén}^2 + \{ (C_{sound}^2 + V_{Alfvén}^2)^2 - 4 C_{sound}^2 V_{Alfvén}^2 \cos^2 \theta_{Bn} \}^{1/2}]$, where θ_{Bn} is the angle between the upstream interplanetary magnetic field (IMF) B , and the shock normal. C_{sound} is sound speed; $V_{Alfvén}$ ($C_{Alfvén}^2 = V_{Alfvén}^2 \cos^2 \theta_{Bn}$) is the Alfvén speed computed from the background magnetic field; hence, $C_{Alfvén}$ is the component of the Alfvén speed in the direction of the shock normal, i.e., in the direction of wave (or shock) propagation. The fast shock Mach number is further calculated as $V^* \cdot n / C_{fast}$. The calculated shock Mach number is further checked for correctness—meaning that the upstream fast Mach number must be larger than one and the downstream fast Mach number must be less than one (i.e., $M_{fast} > 1$ upstream, and $M_{fast} < 1$ downstream).

4. Simulation Results

4.1. Validation of 3-D Global MHD Simulation

Validation of the simulation is done by comparing the simulation result with in situ solar wind parameters [e.g., Wu *et al.*, 2011]. In order to match the IP shock arrival time and the time profile of solar wind parameters at Earth, we adjust a peak speed of 795 km/s and a duration of 50 min for the velocity pulse is used.

Figure 6a shows the comparison between the H3DMHD simulated (red) and ACE measured (black) solar wind parameters. Figures 6a (first panel) to 6a (fourth panel) are proton temperature (T_p), velocity (V), density (n_p),

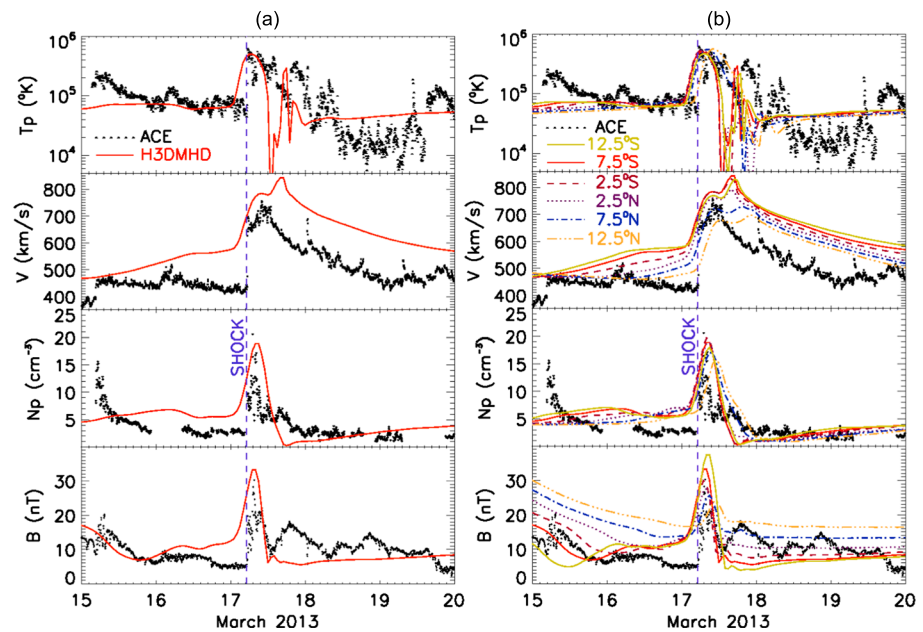


Figure 6. (a) Comparison of H3DMHD simulated (red) and situ measurement data from ACE (black). Figures 6a (first panel)–6a (fourth panel) are proton temperature (T_p), proton speed (V), proton density (N_p), and magnetic field strength (B), respectively. (b) Comparisons of observed ACE in situ measurements (black) with H3DMHD simulated results at different latitudinal locations: 12.5°N (orange dash-dot-dot-dot-dashed lines), 7.5°N (blue dash-dotted lines), 2.5°N (dark-brown dotted lines), 2.5°S (purple dashed lines), 7.5°S (red solid lines), and 12.5°S (green solid lines). Vertical blue-dashed lines indicate the arrival of the IP shock at ACE.

and magnetic field strength (B), respectively. Black dotted lines represent solar wind parameters observed by ACE and red solid lines represent H3DMHD simulation results monitored at 7.5°S of solar equator. (Note that Earth was orbiting around 7.2°S during the period of 15–19 March 2013.) Blue-dashed vertical line indicates the arrival time of the observed IP shock at ACE spacecraft. In general, the simulated solar wind profiles are in reasonable agreement with the observation. While the arrival time of the enhancement in density, upstream of the IP shock was ~ 4 h earlier than the observation, the arrival time of the peak of IP shock's downstream in density and magnetic field matches as well. Actually, the magnitude of IMF, solar wind density, velocity and temperature also show a good match. Many realistic global simulations conducted previously have shown difficulties in matching all parameters with in situ measurements [e.g., Manchester *et al.*, 2004; Odstrcil *et al.*, 2005; Wu *et al.*, 2007a, 2007b, 2011, 2012; Lugaz and Roussev, 2011; Shen *et al.*, 2011; Xie *et al.*, 2012]. Due to the limitation of observation for the input at the inner boundary (at $2.5 R_S$), we consider that our simulation results reasonably match the main feature of the true CME-driven shock.

Figure 6b shows the comparisons of the in situ data with H3DMHD simulation results at different latitudinal locations: 12.5°N (orange dash-dot-dot-dot-dashed lines), 7.5°N (blue dash-dotted lines), 2.5°N (dark-brown dotted lines), 2.5°S (purple dashed lines), 7.5°S (red solid lines), and 12.5°S (green solid lines). It is shown that the simulated shock arrival time at 1 AU was ~ 4 h earlier in the southern area (e.g., red solid curves: data were obtained at 7.5°S) than it was in the northern area (e.g., orange dash-dot-dot-dot-dashed curves: data were obtained at 12.5°N). The source location of the CME on 15 March 2013 was at N11E12. One may wonder why IP shocks arrived earlier in the southern than in the Northern Hemisphere. This is because the IP shock arrival time is affected not only by the location of solar source but also by the background solar wind condition. This result is consistent with previous studies [e.g., Wu *et al.*, 2007b]. For the 15 March 2013 CME event, the background solar wind speed was ~ 100 km/s faster in the Southern Hemisphere (see solid lines) than in the Northern Hemisphere (dot-dashed lines) (see Figure 6b, second panel). The early arrival time of the IP shock at southern monitoring stations (e.g., 12.5°S, 7.5°S, or 2.5°S) was caused by the faster background solar wind speed.

Our input assumptions may be compared to empirical assumptions of varying complexity used by other models (ENLIL, BATS-R-US, etc.) A primary objective is to get the shock time of arrival correct at Earth. Tuning these assumptions can often do the job via minor tweaking. Our arrival of -1 h (modeled minus

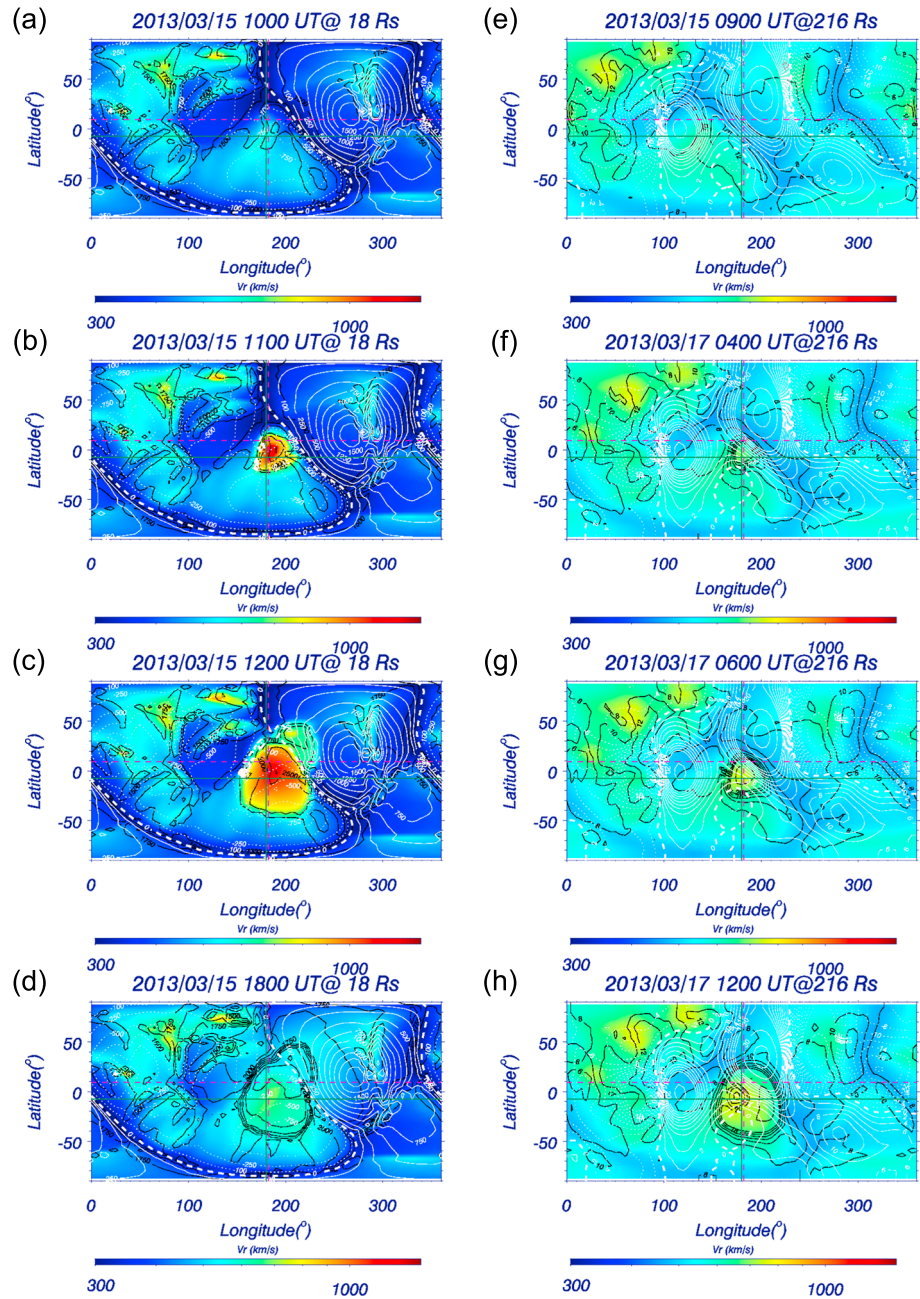


Figure 7. (a–d) The $18 R_S$ solar wind profiles at four times: 10:00, 11:00, 12:00, and 18:00 UT on 15 March 2013. (e–h) The $216 R_S$ solar wind profiles at four times: 09:00 UT on 15 March, 04:00, 06:00, 12:00 UT on 17 March 2013. Color represents solar wind velocity, black contour lines represent solar wind density (units of number cm^{-3}), and white contour lines represent interplanetary magnetic fields (IMFs, units of nT).

observed time) is considered acceptable. The “holy grail” of all models is to mimic all physical fluid and magnetic parameters at designated locations.

Figure 7 shows a time sequence of undisturbed and disturbed solar wind parameters at $18 R_S$ (a–d) and $216 R_S$ (e–h). This is done to examine the locations of the Earth and the flare/CME source locations relative to the sector boundary. Colors represent the velocity profile (color bar shows the scaling of velocity), while black and white contours represent the values of density (unit in number cm^{-3}) and IMF (unit in nT), respectively. Furthermore, we use white solid contours to represent positive magnetic field in the radial direction (B_r), white dotted contours represent negative B_r (inward to the Sun), and white dashed contours are for zero magnetic field

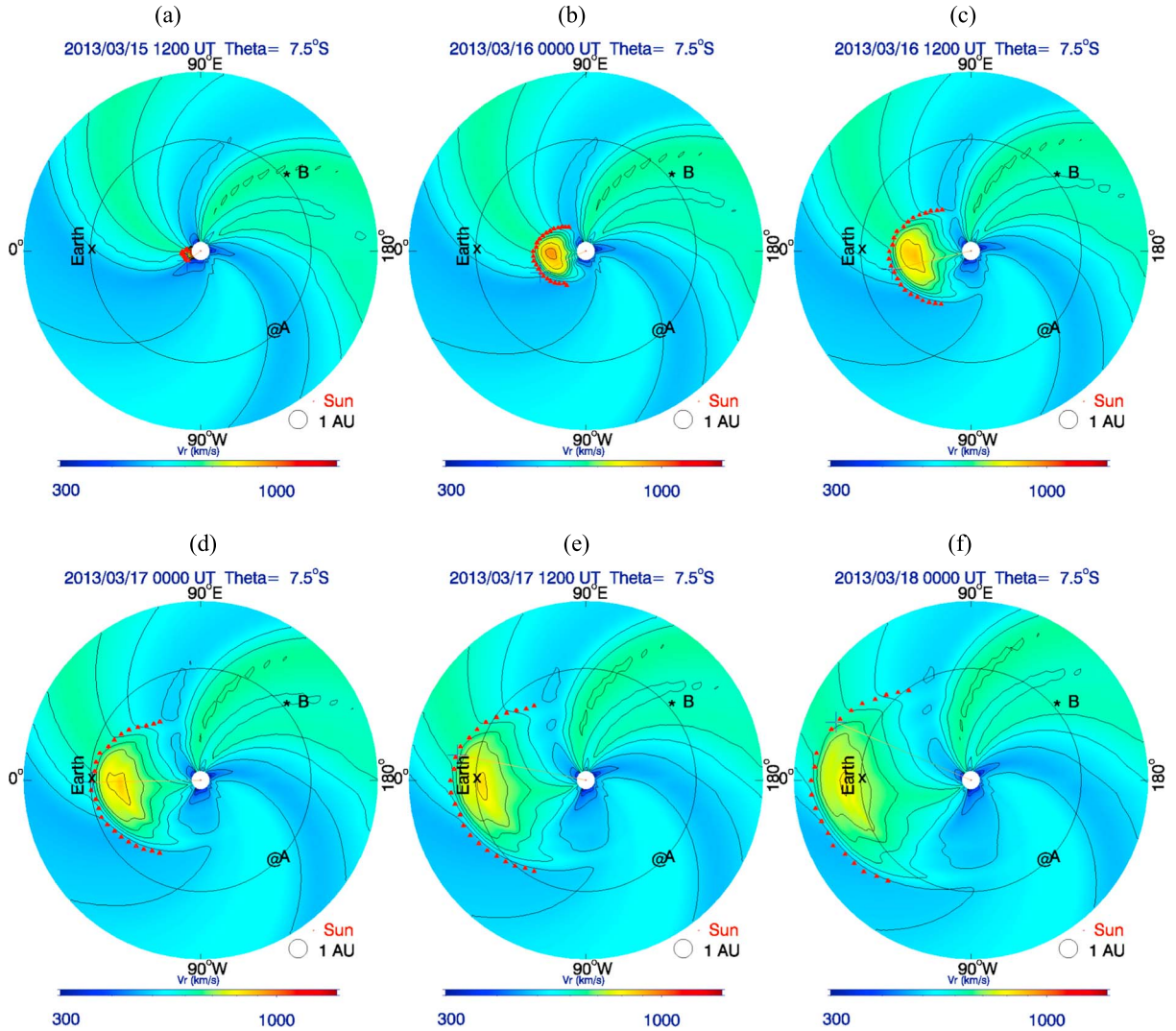


Figure 8. The radial component of solar wind speed ($V_{\text{solar-wind}}$) on the $\theta = 97.5^\circ$ plane in spherical coordinate system (or the $\lambda = 7.5^\circ\text{S}$ plane). The solid circle is at 1 AU ($215 R_S$). Earth is located at heliolongitude, $\phi = 0^\circ$; thus, the east limb (relative to Earth) is at the top, 90°E , and the west limb is at the bottom, 90°W . The outer boundary is at $345 R_S$. At sign and asterisk show positions of STEREO-A and STEREO-B, respectively. Red small triangles (or dots) mean upstream of IP fast shocks or waves.

(or location of heliosphere current sheet, HCS). Figures 7a and 7e show the background (or undisturbed) solar wind profile: Figures 7a–7d show $18 R_S$ solar wind profiles at four times, 10:00, 11:00, 12:00, and 18:00 UT on 15 March 2013, whereas Figures 7e–7h show the solar wind profile at $216 R_S$ at four different times: 09:00 UT on 15 March and 04:00, 06:00, and 12:00 UT on 17 March 2013. The crosses of vertical and horizontal straight purple dashed and green solid lines represent the solar source location and the Earth.

Figures 7a and 7e shows clearly that the Earth and solar flare/CME source locations are located on different sides of the sector boundary (or more precisely, the heliospheric current sheet, HCS): B_r is positive at the Earth (Figures 7e–7h) but is negative at $18 R_S$ (Figures 7a–7d) with 11° north in latitude and 168° in longitude. This corresponds to the site where the solar M1.1 X-ray flare erupted at 05:46 UT. Note that the Earth is located at longitude = 180° and latitude = -7.2° ($S7.2^\circ$). Figure 7b (for time at 11 UT on 15 March) shows the solar wind has been disturbed which may be caused by the IP shock arriving at $18 R_S$. Figures 7c and 7d (for time at 12 and 18 UT on 15 March) show disturbed solar wind (due to IP shock) crossed the northwestern sector boundary (HCS). Figure 7f (time at 04 UT on 17 March) corresponds to the disturbed solar wind (due to the IP shock) arriving at the Earth; Figures 7g and 7h (time at 06, 12 UT on 17 March) show that the IP shock arrived at the Earth. The simulated IP shock arrival time at the Earth matches well (Figure 6) with in situ observations from the ACE spacecraft.

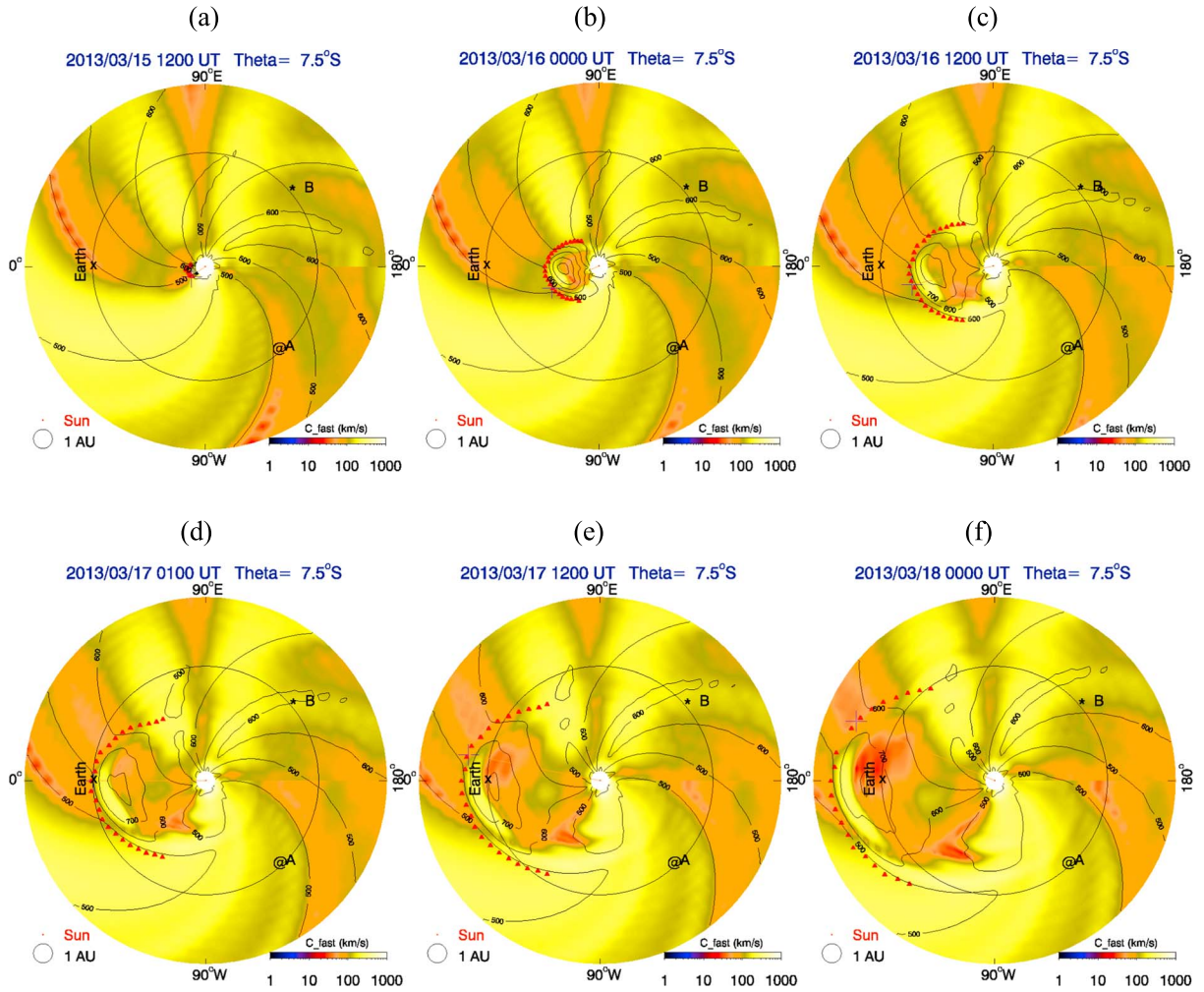


Figure 9. Colors represent the fast-mode speed (C_{fast}) in the $\theta = 97.5^\circ$ plane. The solid circle is at 1 AU ($215 R_S$). Earth is located at heliolongitude, $\phi = 0^\circ$; thus, the east limb (relative to Earth) is at the top, $90^\circ E$, and the west limb is at the bottom, $90^\circ W$. The outer boundary is at $345 R_S$. At sign and asterisk show positions of STEREO-A and STEREO-B, respectively. Red small triangles (or dots) mean upstream of IP fast shocks or waves. Black contour lines represent the speed of solar wind.

Figures 8 and 9 show color contours of solar wind speed ($V_{solar-wind}$) and fast wave speed (C_{fast}), respectively, on the surface of an angular cone at $7.5^\circ S$ that is centered at the Sun's center: for 12:00 UT on 15 March 2013 (Figures 8a and 9a), for 00:00 UT and 12:00 UT on 16 March 2013 (Figures 8b–8c and 9b–9c), for 00:00 UT and 12:00 UT on 17 March 2013 (Figures 8d–8e and 9d–9e), and for 00:00 UT on 18 March 2013 (Figures 8f and 9f). The solid circle is at 1 AU ($215 R_S$). Earth is located at heliolongitude, $\phi = 0^\circ$; thus, the east limb (relative to Earth) is at the top, $90^\circ E$, and the west limb is at the bottom, $90^\circ W$. The outer boundary is at $345 R_S$ (~ 1.6 AU). Black curves are the contours of solar wind velocity. At sign and asterisk mean positions of STEREO-A and STEREO-B spacecraft, respectively. Red dots (in Figure 8) represent upstream of IP shocks that were identified by using the wave tracing method (WTM) [Wu *et al.*, 1996] discussed in section 3.2.

It can easily be seen that Figure 8 shows the highly nonuniform profile of the solar wind on the surface of the angular cone centered at $7.5^\circ S$. The region of higher speed (in yellow-green color) is a so-called stream interaction region [e.g., Burlaga, 1975; Dryer, 1975]. Note that a stream interaction region is a flare-associated stream (see Figure 3 in the previous study of Burlaga [1975]). According to the in situ observation shown in Figure 3, the pressure is high in the region where V is increasing. The region of high density is separated from that of high temperature by a thin boundary called the stream interface (see “SI” marked in Figure 3), and the highest magnetic field intensities follow the high densities [Burlaga, 1975].

4.2. Effect of Background Solar Wind on the IP Shock Acceleration/Deceleration

Using the WTM method (as described in section 3.2), the shock Mach number is computed along the radial direction upstream of the shock. The shock was traced at a number of longitudes, from $\phi = 125^\circ$ to $\phi = 240^\circ$ with an increment of 5° in the plane of latitude $= 7.5^\circ\text{S}$ since the Earth is located at $\phi = 180^\circ$ and $= 7.2^\circ\text{S}$ on 15 March 2013. Due to the limitation of simulation grid size (5°), the angular cone at 7.5°S is the one that is the closest to the Earth.

Figure 10 shows snapshots of various solar wind parameters (V_r , N_p , B , and T) at different times (Figure 10a) and different locations (Figure 10b). The vertical red dotted lines indicate the location for the upstream of IP shocks. Black solid lines, blue dotted lines, red dashed lines, and orange triangle lines represent simulated solar wind velocity in the r direction (V_r), density, magnetic field, and temperature, respectively.

Figures 10a (first panel) to 10a (sixth panel) show solar wind parameters at different times: 12UT on 15 March, 00UT, 12UT on 16 March, 00UT, 12UT on 17 March, and 00UT on 18 March, from the first panel to the sixth panel, respectively. For a forward fast shock, solar wind velocity, density, magnetic field, and temperature all show increases across the shock. Due to the low grid resolution in the simulation, the thickness of the simulated IP shocks is probably not realistic. Increasing the grid resolution may help resolve the shock structure. However, our previous results have shown that simulation with higher grid resolution may cause the overshoot problem in the downstream region [see, e.g., Wu, 2009, Figure 1]. Current MHD models are not capable of simulating the fine shock (or discontinuity) structure (see the comparison in Figure 6). Besides missing the proper dissipation term from the governing equation, numerical methods, such as the numerical scheme, grid resolution, and the initial/boundary conditions, employed in the simulation code can also have a direct effect on the shock stability. This is an issue beyond the scope of this study.

The WTM method has been applied to 1-D simulation results and successfully obtained non-steady IP shock properties from the Sun to the Earth [Wu *et al.*, 1996]. Wu *et al.* [2006] simulated more realistic data and compared simulation results with 1 AU in-situ observation during the 2003 Halloween epoch (4 IP shocks at 1 AU). Wu *et al.* [2006] successfully use WTM to compute the properties of IP shocks on their way to the Earth [see Wu *et al.*, 2006, Figure 9].

Recently, the WTM has been successfully used to provide 3-D simulation results near the Sun [Wu *et al.*, 2012] and in the inner heliosphere [Dryer *et al.*, 2012; Liou *et al.*, 2014]. The restriction of WTM is that it assumes that the IP shock propagates along or near ($<25^\circ$) the r direction as shown in section 3.2. Therefore, we choose a plane ($\theta = 57.5^\circ$) which is close to the Earth position in March 2013. Note that the solar wind speed is variable, e.g., see Figure 3. The Mach number is computed using the IP shock speed in the shock rest frame. The solar wind speed affects the propagation of the IP shock wave since the latter is riding on the background solar wind. Previous studies [e.g., Liou *et al.*, 2014] show that solar wind parameters have a great effect on the shock Mach number. Liou *et al.* have demonstrated that (i) the shock Mach number is not the largest at the nose of the CME and (ii) Mach number is larger in the west than in the east of the CME initiation longitude.

Using the WTM method as described in section 3.2, a set of IP fast shock Mach numbers is computed along the Sun-Earth line ($\phi = 0^\circ$). Repeating the same procedure for 23 times: along different longitudinal directions ($\delta\phi = 5^\circ$ for the angle of $E55^\circ < W60^\circ$). Top to bottom panel of Figure 10b show solar wind parameters at 00 UT on 17 March at different longitudinal locations: $\phi = -40^\circ$ (E40°), -20° (E20°), 0° (E00°), 20° (W20°), 40° (W40°), and 60° (W60°), on the equatorial plane with a latitudinal angle $\theta = -7.5^\circ$ (57.5°). It is clear that the IP shock fronts' propagation speeds are highly nonuniform. (i) IP shock propagated faster near the source location (see Figure 10b, third panel). (ii) Solar wind speed at the IP shock downstream is higher near the source location than the other locations.

Twenty-four sets of Mach numbers are computed at different ϕ angles along the radial direction. Combining these 24 sets time profiles of IP shock Mach numbers, Figure 11a shows the temporal and spatial profile of the IP shock Mach number in colors. The shock Mach number is computed for the period between 10:00 UT on 15 March and 12:00 UT on 19 March 2013. There are five blue curves representing the upstream location of the IP shock (or the fast shock wave front, we will state it as shock hereafter) at five different time instances (red dots in Figures 8a–8e). Each time frame is 12 h apart. The propagating distance from the solar flare/CME source to the 00 UT/03–16 shock propagating distance is much longer than the subsequently

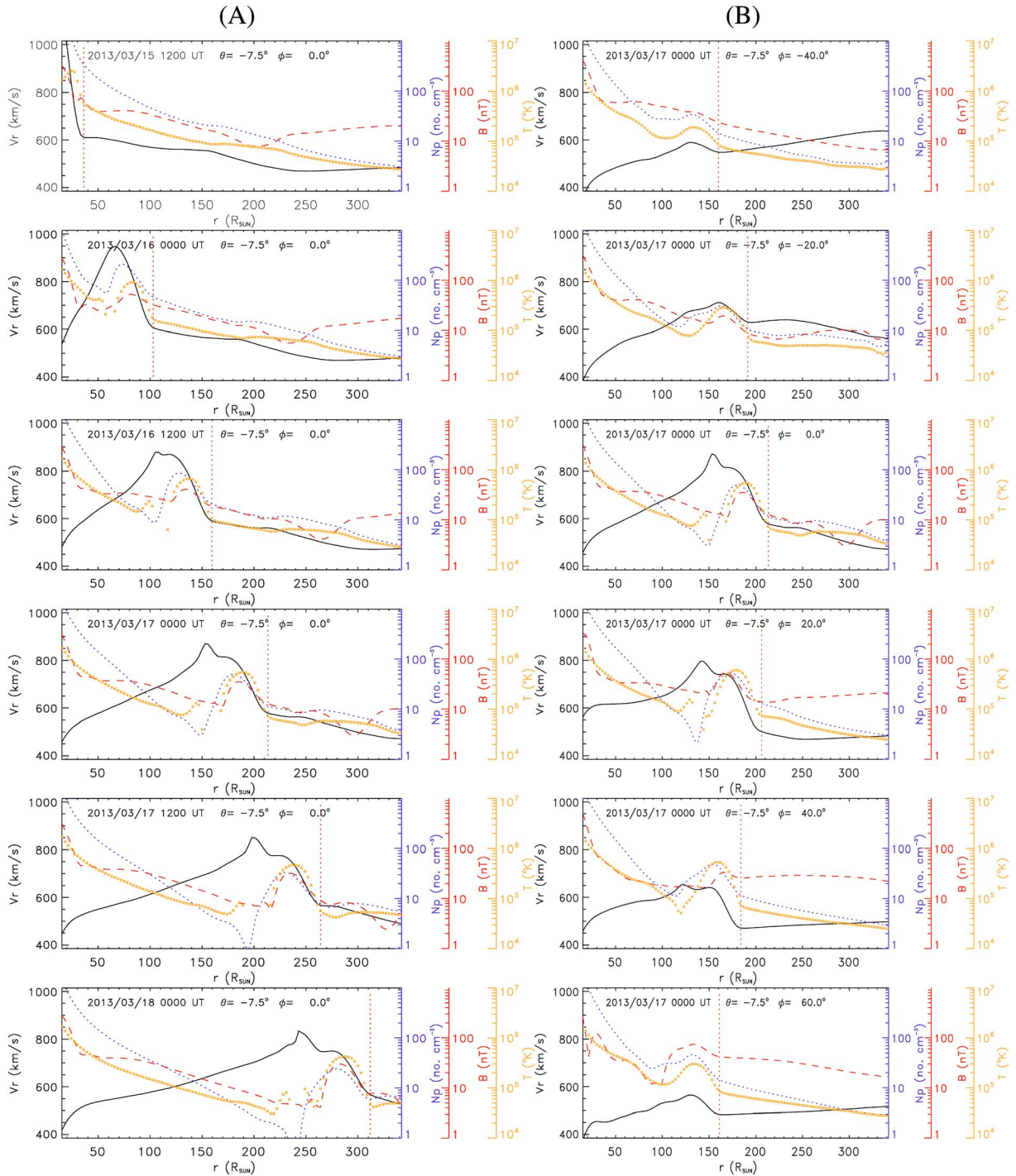


Figure 10. (a, first to sixth panels) Snapshots of solar wind profiles in the Sun-Earth direction ($\theta = 7.5^\circ$ and $\phi = 0^\circ$) at different times: 12 UT on 15 March, 12 UT on 16 March, 00 UT and 12 UT on 17 March, and 00 UT on 18 March, respectively. (b, first to sixth panels) Solar wind profiles at 00 UT on 17 March at different longitudinal locations in the equatorial plane with $\theta = 7.5^\circ$: $\phi = E40^\circ$, $E20^\circ$, $E00^\circ$, $W20^\circ$, $W40^\circ$, and $W60^\circ$, respectively. The black solid, blue dotted, red dashed, and orange triangle curves represent solar wind radial velocity, density, magnetic field, and temperature, respectively. The vertical red dotted line indicates the region upstream of the IP shock.

paired distances as are shown in Figure 11a. It is clear that the IP shock propagation speed close to the Sun is faster than it was near the Earth. It means that the IP shock was slowed down by the slower background solar wind. The IP shock Mach number (e.g., see the red area in Figure 11a) is stronger near the Sun than other places. The IP shock Mach number is highly variable. For example, the strongest IP shock is located in the direction of $\sim 10^\circ$ – 15° W of the Sun-Earth line. Along 10° W of Sun-Earth line, Mach numbers (M_{fast}) are ~ 8 ,

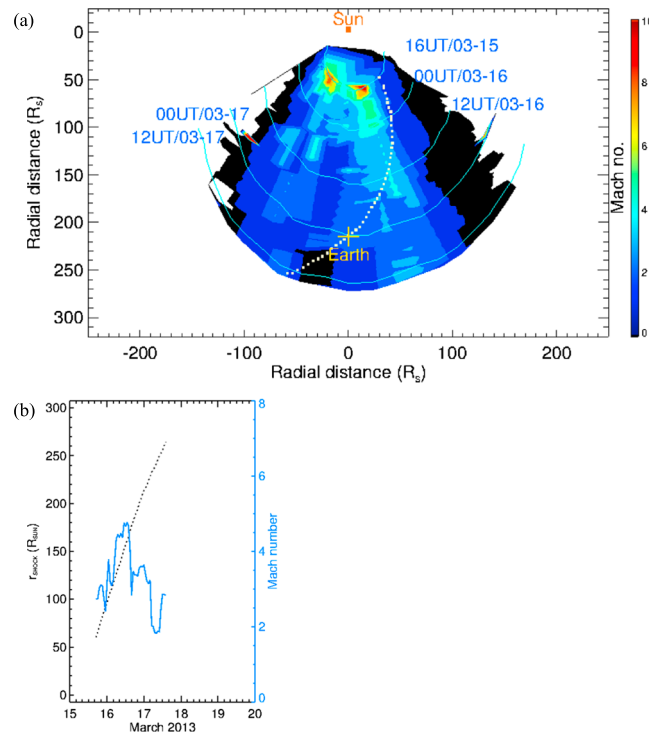


Figure 11. (a) The simulated radial profile of fast-mode shock Mach number in the solar ecliptic plane for the 15 March 2013 CME epoch. The upstream location of the shock at six different times are labeled and represented by contour lines. The location of the Sun and the Earth are marked as red square and plus sign, respectively. The dotted curve represents the cob points (assuming a classical Parker quiet-Sun IMF). (b) Variation of Mach number (blue curve) marked as dots on the left, and the location of the shock (black dotted curve, r distance away from the Sun).

region of increasing fast wave speed, which resulted in the decrease of shock Mach number. In contrast, Figures 9d–9f show that the IP shock was propagating into a region of decreasing fast wave speed, which resulted in the increase of shock Mach number. While the changes in the shock Mach number are not unexpected, it has not been demonstrated before. This result clearly demonstrates that the background solar wind plays an important role in the variations of IP shock strength.

The definition of Mach number is the ratio of the IP shock speed (in the shock frame) to the wave speed (e.g., fast, slow, Alfvén wave speeds). The wave speed depends on the background solar wind condition. The IP shock is stronger in the region with lower wave speed, as demonstrated in Figure 7 of the recent study by Liou *et al.* [2014]. Since ideal MHD (single fluid) is used in this study, electron temperature is not considered in this study. Electron temperature may differ from proton temperature which may affect in the determination of fast-mode velocity. This is an interesting question for the future study.

4.3. Relationship Between Shock Strength and Intensity of SEPs

It has been shown that there is a good linear relationship between the intensity of SEPs measured by ACE and fast-mode shock Mach number, obtained from 1.5-D MHD simulation [Liou *et al.*, 2012, 2013]. Here we investigate this surprising result with more realistic 3-D shock. Figure 12a shows the time-intensity profile of the proton SEP (observation from ACE/SIS as shown in Figure 4) and the IP shock Mach number (derived from the H3DMHD simulation results) for the period of 15–19 March 2013. The blue/red curves are the intensity of SEPs with energy 10–30 and 30–80 MeV, and the black dotted curve is the shock Mach number. The time profiles of these curves are similar. Figure 12b shows the Pearson correlation coefficient (r_{cc}) between the shock Mach number and the proton integral flux of SEPs. The correlation coefficient is 0.566 for energy 30–80 MeV (in red) and 0.124 (in blue) for energy 10–30 MeV. Note that the correlation

6, 4.4, 3.7, and 4.0 at radial distances of 61, 108, 163, 215, and 265 R_S , respectively. Locations of the Sun and the Earth are marked as “■” and “+” sign, respectively.

The white dotted curve represents the upstream location of the IP shock that connects to the Earth by magnetic field lines. Variations of the Mach number (blue curve) and location (r distance away from the Sun) of the IP shock (black dots) are shown in Figure 11b. The Mach number varies in a range between 1.5 and 4.6, and the peak of the Mach number (~ 4.6) occurred when the IP shock was located at $r \sim 170 R_S$ at 13 UT on 16 March 2013.

One may ask why the shock strength increased after 00 UT, 17 March 2013 ($dt = 42$ h). It is well known that the solar wind is highly nonuniform and MHD wave speeds depend on the solar wind parameters. Figure 9, as discussed above, shows the fast wave speed profile at different times. Along the Sun–Earth line (Figure 9a), the fast wave speed was lower near the Sun and the Earth. The Earth is located to the left and marked as a plus sign. Figures 9b and 9c show that the IP shock was propagating into a

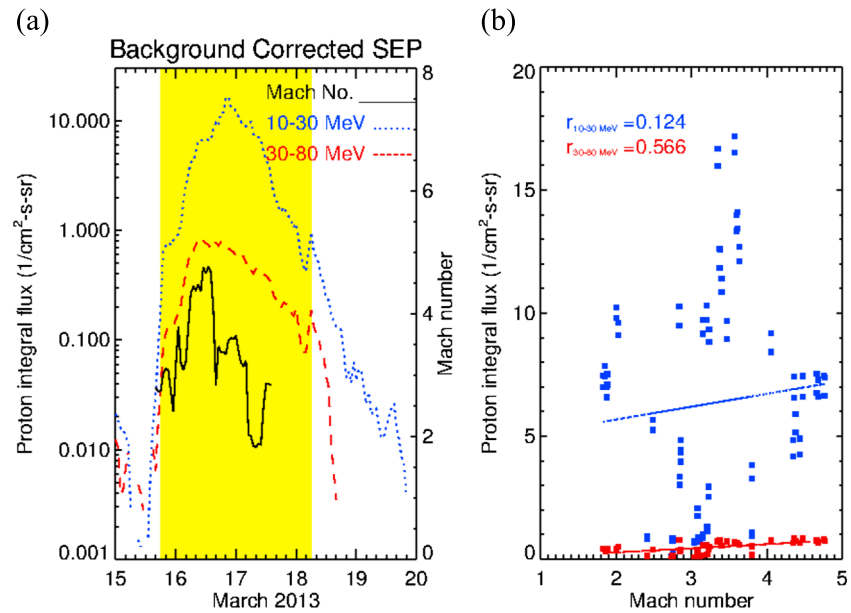


Figure 12. (a) Solar energetic proton flux detected by the Solar Isotope Spectrometer (SIS) on the ACE spacecraft for 10–30 MeV (red) and 30–80 MeV (blue) energy ranges during the period 15–19 March 2013. The simulated fast-mode shock Mach number at the COB points is also plotted (black). (b) Scatter plots showing the relationship between the hourly integral fluxes of SEPs and fast-mode shock Mach numbers for the two energy ranges. The Pearson correlation coefficients (r_{cc}) and best fit linear relationships for each energy range are also shown.

is computed for the shaded period of the data since no SEP enhancement was observed by ACE until ~18 UT on 15 March 2013.

Because the SEP data were collected at ACE away from the source, in order to make a strong connection between the shock strength and the SEP flux, one has to consider possible dependent variables such as the source and transport of SEPs not related to the shock. First is the diverging nature of the solar magnetic field and plasma, which can cause the source of SEP flux (e.g., particles available for shock acceleration or seed particles as some prefer) to decrease radially outward. A radial scaling of the SEP flux should be considered. Here we will consider the scaling factor as a free parameter, and it can be determined with a standard linear correlation analysis by assuming that the correct scaling occurs when the correlation coefficient maximizes.

With all these considered, we correlate the shock Mach number with the SEP flux scaled by different factors: $(215/r)$, $(215/r)^2$, $(215/r)^{2.7}$, $(215/r)^3$, and $(215/r)^4$, where r refers to the radial distance of simulated IP shocks from the Sun. We will refer the scaling factors to r^{-1} , r^{-2} , $r^{-2.7}$, r^{-3} , and r^{-4} for simplicity. Table 1 summarized the correlation coefficients (r_{cc}) between Mach number of IP shocks and measured/scaled SEP intensities. Figures 13a–13e show the scaled SEP fluxes for 10–30 MeV (blue) and 30–80 MeV (red) protons. In general, the scaling moves the flux peak to an earlier time for a smaller power index. To study the relationship between the proton fluxes and the Mach number, we plot the hourly SEP data against their coincident hourly Mach number in Figures 13f–13j. It is quite obvious that the correlation improves for 10–30 MeV with a larger power index. The best correlation ($r_{cc} = 0.73$) occurs when the flux is scaled with $r^{-3.0}$. On the other hand, the correlation for 30–80 MeV becomes poorer for increasing the power index. The largest correlation coefficient occurs for $r^{-1.4}$ ($r_{cc} = 0.82$). Notice that even the $r^{-2.7}$ is a comfortable scaling factor to use for both 10–30 and 30–80 MeV SEPs ($r_{cc} > 0.69$) (Table 2).

Table 1. Correlation Coefficients Between Fast Mach Number of IP Shocks and Measured/Scaled SEP Intensities

Scaled With	r^0	r^{-1}	r^{-2}	$r^{-2.7}$	r^{-3}	r^{-4}
10–30 MeV	0.124	0.331	0.589	0.717	0.728	0.511
30–80 MeV	0.566	0.783	0.795	0.688	0.620	0.352

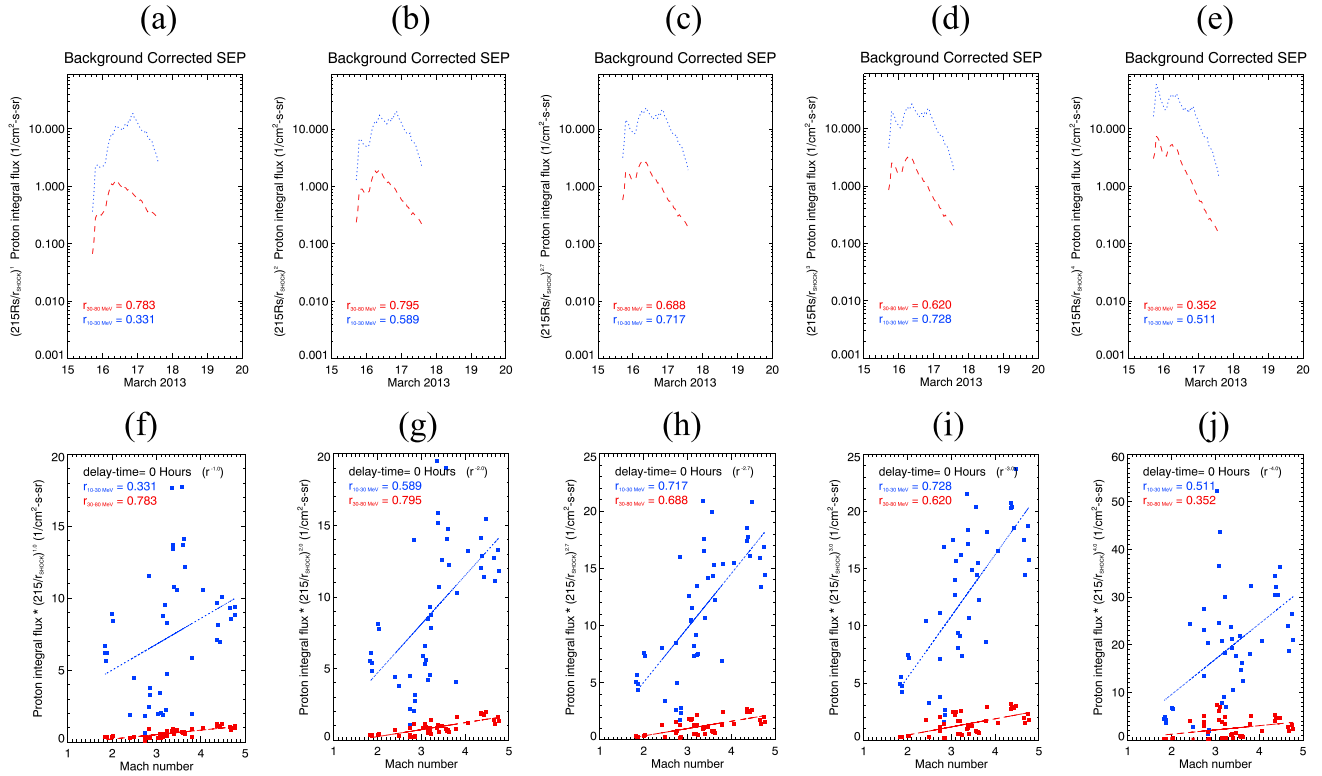


Figure 13. (a–e) The scaled time-intensity profile of solar energetic particles integral flux (hourly resolution) by ACE/SIS for SEP particles of 10–30 (blue dotted curves) and 30–80 (red dashed curves) MeV during the period 15–19 March 2013. (f–j) Correlation coefficients between the IP fast-mode shock Mach number and the scaled SEP flux. The scaling factors, from left to right, are r^{-1} , r^{-2} , $r^{-2.7}$, r^{-3} , and r^{-4} .

Another important factor one needs to consider is a possible delay of SEPs caused by transport. To determine the delay time, we will use time-lagged cross correlation. Here we will use a scaling factor $r^{2.8}$ for 10–30 MeV protons and $r^{-1.4}$ for 30–80 MeV protons, as suggested from the previous result, and the result is shown in Figure 14. For 10–30 MeV protons, the correction coefficient does not vary much, and it does not drop below 0.7 within a few hours. For 30–80 MeV protons, the maximum correlation coefficient occurs at no delay, and the correlation coefficient decreases monotonically with the delay time.

5. Discussion

5.1. Effect of Sector Boundary on the SEP Profile

It is well known that CME-driven shocks are an important source of energetic particles in the heliosphere. Gradual solar energetic particles are associated with shocks driven by coronal mass ejections [e.g., *Kahler et al.*, 1978]. Observations of the intensity of SEP events at 1 AU often reveal a longitudinal structure [Cane et al., 1998]. For a western event (flare or CME) the SEP flux shows sharp increases within a couple of hours after the event onset owing to the typical Parker spiral field. For an eastern event, SEP flux increases slowly with a much longer delay time. Near the central meridian of the Sun the typical SEP flux

Table 2. Best Correlation Coefficient for Shocks' Fast Mach Number Versus Time-Delayed SEP Intensities

Scaled With	r^0	r^{-1}	r^{-2}	$r^{-2.7}$	r^{-3}	r^{-4}
10–30 MeV	0.910 ^a (11) ^b	0.865 (10)	0.788 (7)	0.741(1)	0.728 (1)	0.545 (0)
30–80 MeV	0.770 ^a (4) ^b	0.860 (0)	0.846(0)	0.741(0)	0.675 (0)	0.407 (0)

^aBest correlation coefficient (c.c) picked from 14 delay-time c.c.s' as shown in Figure 14.

^bDelay-time (unit in hours) with the best c.c.

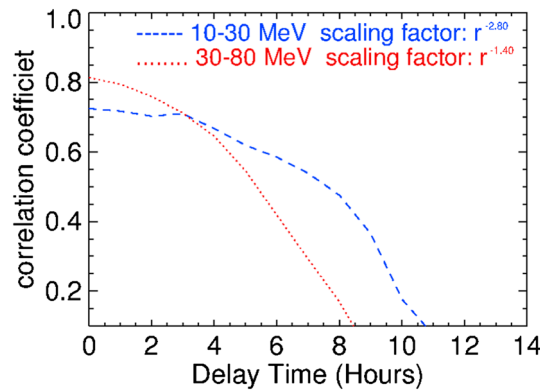


Figure 14. Time-lagged cross-correlation coefficients between the time profile of the Mach number and the radially scaled SEP intensities for 10–30 MeV ($r^{-2.8}$, blue-dashed line) and 30–80 MeV ($r^{-1.4}$, red-dotted line).

spot near the center in Figure 7b). One hour later (12UT on 15 March, Figure 7c), the flank of the CME expanded across the sector boundary (the white dashed line) northwest of the Sun-Earth line direction. Particles accelerated at the IP shock may be able to propagate along the IMF to the Earth after the IP shock has crossed the sector boundary and emerged into the same magnetic sector as Earth's. This would explain the ~12 h delay time of the SEP flux at ACE. Earlier studies have shown that sector boundaries may inhibit the propagation of energetic particles across magnetic field lines [e.g., *Svestka et al.*, 1976; *Zeldovich and Kuzhevskij*, 1981; *Khabarova et al.*, 2015a]. *Khabarova et al.* [2015a, 2015b] also found that interactions of ICMEs with the HCS can lead to significant particle acceleration due to plasma confinement.

Observations show that CMEs are deflected not only in the corona but also in the interplanetary medium [e.g., *Wang et al.*, 2014]. On the other hand, the statistical study of *Kahler et al.* [1996] showed that the streamer structure has no detectable effect on the development of the shock and CME driver. Note that *Kahler et al.* [1996] used potential field results ballistically projected to the Earth with the solar rotation considered. Such a method ignores an important fact that the solar wind is a compressible fluid and therefore cannot reasonably reconstruct the realistic magnetic field structure in the heliosphere. Recently, a statistical study of 130 shock events by *Zhao et al.* [2007] indicates that the shocks associated with flares near the HCS have a lower probability of reaching the Earth. They also demonstrated that the shocks associated with solar flares located on the same side of the HCS as the Earth have a greater chance to reach the Earth than those shocks with the associated flares on the opposite side. More recently, *Agueda et al.* [2013] investigated three large near-relativistic (>50 KeV) electron events observed in 2001 by both the ACE and the Ulysses spacecraft and found that the HCS could be playing a role in near-relativistic electron release and regulating the characteristics of the electron injection profiles. Results of the present study show clearly that the HCS can act as a barrier to SEP propagation.

It is worth mentioning that ACE recorded a significant SEP enhancement at ~05UT on 16 March 2013 (see Figure 4), but not a single type II was observed. We also call attention that several small flares from active region 1698 appeared during that period: (1) 03:53/04:19/04:08/ B.8/S21W48 (start/end/peak-time/flare class/flare location); (2) 04:20/04:32/04:28/C2.6/ S17W48; (3) 04:52/06:25/05:39/ C2.8/ S22W49; and (4) 04:54/06:30/05:30/C2.7/S22W49. One may argue that the small SEP enhancement at ~04 UT was associated with these flares; however, we do not think those small flares are the source that generated the larger SEP enhancement seen later because they are not well connected to ACE.

The derived time-dependent profile of the shock Mach number at the ACE foot points (Figure 11 and solid curve in Figure 12a) from the simulation results shows clearly that the large SEP enhancement coincided with the increase of the IP shock Mach number and the 30–80 MeV SEP flux is generally well correlated (see Figure 12a), with $r_{cc} = 0.566$ (see Figure 12b). However, there is no correlation for the lower energy (10–30 MeV) protons (see Figure 12b, with $r_{cc} = 0.124$).

in a large event increases slowly after the onset of the solar event, reaches a peak when an IP shock crosses the spacecraft and decreases after the IP shock crossing.

The SEP event shown in Figure 4 is a typical Sun-Earth line event but with a ~12 h delay time. This is because the interplanetary magnetic field (IMF) was not well connected between ACE and the leading edge of the initial IP shock. Figure 6 shows clearly that the CME source region and the Earth are located in different magnetic sectors: IMF was negative near the CME source region (see Figure 6a at ~18 R_S) but positive at the Earth (see Figure 6b, at ~216 R_S).

By examining Figures 7b, 7c, 7f, and 7g, one can conclude that the leading edge of the ICME arrived at 18Rs at 11UT (see the red high-speed

5.2. Effect of Shock Mach Number on the SEP Profile

It is generally accepted that IP shocks are a major source of SEPs in the heliosphere. For a steady and planar shock, the diffusive shock acceleration theory predicts that an increase in the shock compression ratio hardens the SEP spectra downstream of the shock and an exponential flux increase toward the shock from shock upstream. Observational tests of the theory are complicated by the facts that SEP particles may come from different parts of the shock (often called COBpoints: Connection with Observer points) encountered by the spacecraft. Some previous studies have generally concluded that the varying time-intensity profile of low-energy (< 10 MeV) SEP during the shock passage is associated with different types of shocks [Van Nes *et al.*, 1984; Kallenrode, 1995; Lario *et al.*, 1995]. However, with more energy coverage and shock events, Lario *et al.* [2005] concluded that “There is a trend for faster and stronger shocks to have greater effects on the energetic particle intensities. However, the parameters of the shock do not determine unequivocally the characteristics of the energetic particle event observed at the passage of the shock.” On the other hand, for high-energy (> 10 MeV) SEPs, some earlier studies seem to suggest a shock-SEP connection. For example, there is a good correlation between proton (> 2 MeV n^{-1}) peak intensities and the speed of their associated CMEs [e.g., Kahler, 2001]. The SEP peak flux (> 10 MeV n^{-1}) is better correlated with the CME speed than with the X-ray flare peak flux [Gopalswamy *et al.*, 2003]. Recently, Liou *et al.* [2012] derived the fast-mode shock Mach number from a 1.5-dimensional MHD simulation for a series of CME events on 28 October 2003, the Halloween 2003 epoch, and found that the time series of solar energetic (> 7.3 MeV n^{-1}) oxygen fluxes follows nicely with the trend of the time series of simulated forward fast-mode shock Mach numbers [Liou *et al.*, 2012]. A good linear relationship between the time-intensity profile of ^4He ($E > \sim 10$ MeV n^{-1}) and O ($E > \sim 10$ MeV n^{-1}) and the time profile of concurrent fast shock Mach number was found in a recent study [Liou *et al.*, 2013] for the same events.

In this study we have extended the computation of shock strength to two dimensions (2-D) in the solar ecliptic plane by using simulation results from a global, 3-D time-dependent, MHD simulation with realistic solar wind structures. The strength of the IP shock is highly nonuniform (see Figure 11) and depends on the solar source location and the background solar wind conditions (e.g., see Figures 8 and 9). We have assumed that particles propagate along a spiral magnetic field by tracing from the Earth back to the CME-driven shock. Our result indicating a better correlation between the shock Mach number and the high-energy SEP flux is consistent with the results of Liou *et al.* [2012, 2013], indicating that shock Mach number is an important parameter in studying particle acceleration by shocks. The present study also suggests a new approach to predict the intensity of SEP flux. The correlation coefficients obtained from the present work are ~ 0.8 , which means approximately 80% of variances in the SEP flux can be predicted by the shock Mach number. Since SEP fluxes are also dependent on the ambient plasma density, which varies from one event to the other, inclusion of this parameter can perhaps improve the prediction. Of course, other factors such as the location and strength of solar sources will also need to be considered. By running a large number of events, it may be possible to build an empirical model that is capable of predicting SEP fluxes at 1 AU with simple input from coronagraph images and GOES X-ray data.

The finding that a good linear relationship exists between SEP flux and shock Mach number is, to some extent, consistent with the Diffuse Shock Acceleration (DSA) model (see the review of, e.g., Jones and Ellison [1991] and Lee [1997]). The DSA model predicts a power law in momentum with the power index $= 3\kappa/(\kappa - 1)$, where κ is the shock compression ratio ($\kappa = v_1/v_2$, v_1 = upstream speed and v_2 = downstream speed). The larger the compression ratio, the harder the spectrum the shock creates. In the MHD theory, the compression ratio is a monotonically increasing function of the shock Mach number if the adiabatic index is constant. Therefore, a larger value of the Mach number corresponds to a large value of κ , which approaches asymptotic limit defined by $(\kappa + 1)/(\kappa - 1)$ for large Mach number. Therefore, our result suggests increases in the SEP flux with the compression ratio. However, there are a number of reasons for the use of the Mach number instead of the compression ratio in the present study. First, the compression ratio cannot be easily calculated because one cannot uniquely determine the downstream from the upstream in 3-D (or even 2-D) shocks. This can be easily done in 1-D. Second, from the energy point of view, the square of the Mach number is roughly the ratio of the kinetic energy of the upstream flow to the sum of thermal and magnetic energy. Therefore, a larger Mach number implies that there is more free energy available for particle acceleration. (A larger Mach number implies a bigger compression when the shock is propagating along a certain direction.) This justifies our approach by correlating SEP flux with the Mach number. Indeed our result supports this view. Furthermore,

unlike the shock compression ratio, the shock Mach number is fundamental in MHD theory that specifies all of the physical parameter changes (v_2/v_1 , n_2/n_1 , B_2/B_1) across the shock. It also infers the field polarity; hence, fast-slow and acoustic modes are taken into account. The result of this study simply serves as an indication that shock strength (or Mach number) is a useful variable for studying the evolving of SEP flux. In the future, a more conclusive study should be undertaken with more events and more accurate methodology to confirm the importance of the influence of shock strength on the SEP flux.

5.3. Radial Scaling and Time Delay of SEP Flux

Our cross-correlation analysis indicates that an improved correlation coefficient can result when the SEP flux is scaled by radial distance from Sun with certain power. However, the scaling is somehow different for the two energy ranges studied. The optimal radial scaling power index is ~ -3 (i.e., r^{-3}) for 10–30 MeV protons, whereas it is smaller (-1 or -2) for 30–80 MeV. Previous studies have shown a radial dependence of SEP (proton) flux peaks and fluencies. However, there is no agreement between the form of radial dependence. For example, *Hamilton* [1988] and *Shea et al.* [1988] suggested a radial scaling form for 10–70 MeV proton fluxes from r^{-3} to r^{-2} for $r < 1$ AU, where r is the heliocentric radial distance in AU. Later using Helio-1 and Helio-2 and IMP 8 data, *Lario et al.* [2006] found that the radial dependence of proton peak fluxes scale with $r^{-2.7}$ for 4–13 MeV and $r^{-1.9}$ for 27–37 MeV. In general, these studies suggest that there is an r dependence in the SEP flux, and the dependence changes with SEP energies [*Ruzmaikin et al.*, 2005]. Our results seem to support such a conclusion, with smaller (larger) r scaling for higher (lower) energy protons.

The r scaling of SEP can be attributed to a number of factors. Theoretically, the diverging IMF will cause SEP flux to decrease as r^{-2} for radially outward field. In addition, if shock acceleration is local, particle abundance around the shock will also affect SEP flux at remote sites. This is usually understood as seed particles in particle injection models. If seed particles are the superthermal solar wind, their density would also decrease with increasing r^{-2} . However, the IMF is not radially outward but spirally out (Parker spiral), the combined effect is that SEP flux measured at different radial distance from the source (i.e., the shock) will present an r dependence with the power index less than -4 . Other possible effects such as convection of the solar wind and adiabatic deceleration, and particle scattering have been discussed previously [e.g., *Ruffolo*, 1995; *Kallenrode*, 2001; *Lario et al.*, 2007; *Zhang et al.*, 2009]. There is little doubt that adiabatic deceleration takes place and the effect would increase the r scaling factor. However, the magnitude of the effect is still not known, especially at the energies of interest here. For example, most previous theoretical studies [e.g., *Ruffolo*, 1995; *Kallenrode*, 2001; *Lario et al.*, 2007] suggest that these effects are not important for protons with energies greater than 1 MeV, except *Zhang et al.* [2009] who suggested that adiabatic deceleration can occur for >10 MeV protons. Particle scattering by small-scale magnetic fluctuations will not only extend the time from particle escape at the shock to the time of detection at 1 AU but will also produce back-streaming SEP flux. While our MHD simulation cannot distinguish between these effects, they are all folded into our r scaling approach and the result is in reasonably good agreement with observations.

Lastly, it is necessary to point out that the present analysis is based on hourly SEP data and their corresponding hourly Mach number derived from our H3DMHD simulation. One may argue that shock acceleration process takes a finite time and therefore should be related to shock properties averaged over the characteristic acceleration time, rather than to the instantaneous shock properties. Many previous observations have shown that SEPs can be produced within 1 h of flare eruption. After the eruption, SEPs are observed continuously over a few days depending on the propagating of the CME-driven shock. Therefore, the use of hourly data for the present study is a reasonable compromise choice. More in situ spacecraft monitors near Earth would be necessary before operational radiation forecasting, in partnership with modeling such as noted here, could be considered.

6. Conclusions and Remarks

The enhancement of proton SEP flux associated with the CME event on 15 March 2013 was observed by two spacecraft at ~ 1 AU spaced 140° azimuthally. According to the observations, STEREO-B observed an increase in electron flux, though only moderately, near simultaneously with the flare peak (~ 7 UT) and a small gradual increase in the low energy (1.1–2 MeV) protons at around 11 UT. On the other hand, ACE observed SEPs ~ 12 h (~ 20 UT, 15 March 2013) after the onset of the CME even though the CME was initiated near the Sun–Earth line. Another 9 h later, ACE observed a large SEP flux enhancement, presumably associated with the same CME event.

In this study we have used our H3DMHD simulation model to investigate the unusual proton SEP observed at ACE. For the two proton energy ranges (10–30 and 30–80 MeV) considered here, our results suggest the following scenario. Upon the CME onset, the magnetic sector boundary, which separated the Earth and the CME onset, may have caused the major SEP flux from reaching the ACE in the earlier stage of the CME development until the CME had expanded over/across the same magnetic sector as the Earth. After that, ACE became well connected to the CME-driven shock and observed a large CME enhancement.

The present simulation study result also demonstrates that at least the fast-mode shock Mach number at the cobpoints can predict ~50% of variances in the proton SEP flux when scaled radially by $r^{-2.8}$ for 10–30 MeV and $r^{-1.4}$ for 30–80 MeV. For space weather prediction, (i) the best correlation ($r_{cc} = 0.73$) occurs when the flux is scaled with $r^{-2.8}$ for 10–30 MeV particles and (ii) the largest correlation coefficient occurs for $r^{-1.4}$ ($r_{cc} = 0.82$) for 30–80 MeV particles. While the present study does not provide a physical interpretation, this result, along with previous ones, strongly suggests that fast-mode shock Mach number is an important parameter in SEP particle production.

The background solar wind is an important factor in the variation of IP shock strength thus plays an important role in manipulation of SEP flux. Finally, we believe that the H3DMHD hybrid simulation model can provide a powerful tool to link the general observations of SEP events observed at 1 AU to their solar sources, as well as to identify the origins of shock formation due to CME and CME/CIR interactions.

Acknowledgments

The simulation results (~7 GB of data) of this study can be obtained through making a request to the lead author. All data used in this study are obtained from public domain. We thank the Wind and ACE PI teams and National Space Science Data Center at Goddard Space Flight Center, National Aeronautics and Space Administration for their management and providing solar wind plasma and magnetic field data; STEREO and LASCO PI teams for providing coronal images; and Kyoto University for providing geomagnetic activity index (*Dst*). We thank Olga Malandraki for her constructive suggestions. We also thank Y.M. Wang (NRL) who provided derived solar magnetic fields at $2.5 R_{\text{SUN}}$. This study is supported partially by Chief Naval Research (CCW, SP), NASA (AV), and NSF base program (KL), AGS1153323 (STW). The Caltech effort was supported by NASA grants NNX13A66G and NNX11A075G. The Hakamada-Akasofu-Fry solar wind model version 2 (HAFv2) was provided to NRL/SSD by a software license from Exploration Physics International, Inc. (EXPI).

References

- Agueda, N., R. Vainio, S. Dalla, D. Lario, and B. Sanahuja (2013), Current sheet regulation of solar near-relativistic electron injection histories, *Astrophys. J.*, 765(83), 9 pp.
- Arge, C. N., and V. Pizzo (2000), Improvement in the prediction of solar wind conditions using near-real time solar magnetic field updates, *J. Geophys. Res.*, 105, 10,465–10,479.
- Berdichevsky, D. B., D. V. Reames, C.-C. Wu, R. Schwenn, R. P. Lepping, R. J. MacDowall, C. J. Farrugia, J.-L. Bougeret, C. Ng, and A. J. Lazarus (2009), Exploring the global shock scenario at multiple points between sun and earth: The solar transients launched on January 1 and September 23, 1978, *Adv. Space Res.*, 43, 113–119, doi:10.1016/j.asr.2008.03.026.
- Burlaga, L. F. (1975), Interplanetary streams and their interaction with the Earth, *Space Sci. Rev.*, 17, 327–352.
- Burlaga, L. F., E. C. Sittler Jr., F. Mariani, and R. Schwenn (1981), Magnetic loop behind an interplanetary shock—Voyager, Helios, and IMP 8 observations, *J. Geophys. Res.*, 86, 6673–6684.
- Cane, H. V., I. G. Richardson, and O. C. StCyr (1998), The interplanetary events of January–May, 1997 as inferred from energetic particle data, and their relationship with solar events, *Geophys. Res. Lett.*, 25, 2517–2520.
- Detman, T., Z. Smith, M. Dryer, C. D. Fry, C. N. Arge, and V. Pizzo (2006), A hybrid heliospheric modeling system: Background solar wind, *J. Geophys. Res.*, 111, A07102, doi:10.1029/2005JA011430.
- Detman, T. R., M. Dryer, T. Yeh, S. M. Han, and S. T. Wu (1991), A time-dependent, three-dimensional MHD numerical study of interplanetary magnetic draping around plasmoids in the solar wind, *J. Geophys. Res.*, 96, 9531–9540.
- Dryer, M. (1975), Interplanetary shock waves—Recent developments, *Space Sci. Rev.*, 17, 277–325.
- Dryer, M., K. Liou, C.-C. Wu, S. T. Wu, N. Rich, S. P. Plunkett, L. Simpson, C. D. Fry, and K. Schenk (2012), Extreme fast coronal mass ejection on 23 July 2012, SH44B-04, AGU Fall meeting, San Francisco, December 3–7.
- Fry, C. D., W. Sun, C. S. Deehr, M. Dryer, Z. Smith, S.-I. Akasofu, M. Tokumaru, and M. Kojima (2001), Improvements to the HAF solar wind model for space weather predictions, *J. Geophys. Res.*, 106(A10), 20,985–21,001, doi:10.1029/2000JA000220.
- Gopalswamy, N., S. Yashiro, A. Lara, M. L. Kaiser, B. J. Thompson, P. T. Gallagher, and R. A. Howard (2003), Large solar energetic particle events of cycle 23: A global view, *Geophys. Res. Lett.*, 30(12), 8015, doi:10.1029/2002GL016435.
- Hamilton, D. C. (1988), The radial dependence of the solar energetic particle flux, in *Jet Propulsion Lab., California Inst. of Tech., Interplanetary Particle Environment. Proceedings of a Conference (SEE N89-28454 22-90)*, pp 86–90.
- Han, S. M. (1977), A numerical study of two dimensional time-dependent magnetohydrodynamic flows. In: PhD thesis, Univ. of Alabama in Huntsville.
- Han, S. M., S. T. Wu, and M. Dryer (1988), A three-dimensional, time-dependent numerical modeling of super-sonic, super-Alfvénic MHD flow, *Comput. Fluids*, 16, 81–103.
- Jones, F. C., and D. C. Ellison (1991), The plasma physics of shock acceleration, *Space Sci. Rev.*, 58(3–4), 259–364.
- Kahler, S. W. (2001), The correlation between solar energetic particle peak intensities and speeds of coronal mass ejections: Effects of ambient particle intensities and energy spectra, *J. Geophys. Res.*, 106, 20,947–20,955, doi:10.1029/2000JA002231.
- Kahler, S. W., E. Hildner, and M. A. I. Hollebeke (1978), Prompt solar proton events and coronal mass ejections, *Solar Phys.*, 57, 429–443, doi:10.1007/BF001060116.
- Kahler, S. W., E. W. Cliver, H. V. Cane, R. E. McGuire, R. G. Stone, and N. R. Sheeley Jr. (1986), Solar filament eruptions and energetic particle events, *Astrophys. J.*, 302, 504–510, doi:10.1086/164009.
- Kahler, S. W., E. W. Cliver, H. V. Cane, R. E. McGuire, R. G. Stone, and N. R. Sheeley Jr. (1987), Solar energetic proton events and coronal mass ejections near solar minimum, in *Proceedings of the 20th International Cosmic Ray Conference Moscow*, vol. 3, p.121.
- Kahler, S. W., J. M. Kunches, and D. F. Smith (1996), Role of current sheets in the modulation of solar energetic particle events, *J. Geophys. Res.*, 101, 24,383–24,391.
- Kallenrode, M.-B. (1995), Particle acceleration at interplanetary shock-observations at a few tens of keV vs some tens of MeV, *Adv. Space Res.*, 15(8/9), 375–384.
- Kallenrode, M.-B. (2001), Charged particles, neutrals, and neutrons, in *Solar Encounter. Proceedings of the First Solar Orbiter Workshop, Puerto de la Cruz, Tenerife, Spain*, edited by B. Battrick and H. Sawaya-Lacoste, ESA SP-493, ESA Publ. Div., Noordwijk, Netherlands, 14–18 May.

- Khabarova, O., G. P. Zank, G. Li, J. A. le Roux, G. M. Webb, A. Dosch, and O. E. Malandraki (2015a), Small-scale magnetic islands in the solar wind and their role in particle acceleration: I. Dynamics of magnetic islands near the heliospheric current sheet, *Astrophys. J.*, **808**(2), 13.
- Khabarova, O., G. P. Zank, G. Li, J. A. le Roux, G. M. Webb, O. E. Malandraki, V. V. Zharkova (2015b) Dynamical small-scale magnetic islands as a source of local acceleration of particles in the solar wind, *J. Phys. Conf. Ser.*, **642**(1), 012033.
- Lario, D., B. Sanahuja, and A. M. Heras (1995), Energy spectrum of low-energy fluxes of particles accelerated by interplanetary shocks, *Adv. Space Res.*, **15**(8/9), 289–292.
- Lario, D., Q. Hu, G. C. Ho, R. B. Decker, E. C. Roelof, and C. W. Smith (2005), Statistical properties of fast forward transient interplanetary shocks and associated energetic particle events: ACE observations, in *Solar Wind 11*, vol. 81, edited by B. Fleck and T. Zurbuchen, Eur. Space Agency, ESA SP-592.
- Lario, D., M.-B. Kallenrode, R. B. Decker, E. C. Roelof, S. M. Krimigis, A. Aran, and B. Sanahuja (2006), Radial and longitudinal dependence of solar 4–13 MeV and 23–37 MeV Proton peak intensities and fluences: Helios and IMP 8 observations, *Astrophys. J.*, **653**, 1531–1544.
- Lario, D., A. Aran, N. Agueda, and B. Sanahuja (2007), Radial dependence of proton peak intensities and fluences in SEP events: Influence of the energetic particle transport parameters, *Adv. Space Res.*, **40**(3), 289–294.
- Lax, P. D., and B. Wendroff (1960), Systems of conservation laws, *Comm. Pure. Appl. Math.*, **13**, 217–237.
- Lee, M. A. (1997), Particle acceleration and transport at CME-driven shocks, in *Coronal Mass Ejections, Geophys. Monog.*, vol. 99, edited by N. Crooker, J. A. Jockelyn, and J. Feynman, 227 pp., AGU Press, Washington, D. C.
- Lemen, J. R., et al. (2012), The Atmospheric Imaging Assembly (AIA) on the Solar Dynamics Observatory (SDO), *Sol. Phys.*, **275**, 17–40.
- Liou, K., C.-C. Wu, M. Dryer, S. T. Wu, D. B. Berdichevsky, S. Plunkett, R. A. Mewaldt, and G. M. Mason (2012), Relationship between solar energetic oxygen flux and MHD shock mach number, in *Physics of the Heliosphere: A 10 Year Retrospective, Proc. 10th Annual Int. Astrophys. Conference, AIP Conf. Proc.*, vol. 1436, pp. 253–258.
- Liou, K., C.-C. Wu, M. Dryer, S.-T. Wu, D. B. Berdichevsky, S. Plunkett, R. A. Mewaldt, and G. M. Mason (2013), Magnetohydrodynamic fast shocks and their relation to solar energetic particle event intensities, *Terr. Atmos. Oceanic Sci.*, **24**(2), 165–173, doi:10.3319/TAO.2012.05.08.01.
- Liou, K., C.-C. Wu, M. Dryer, S.-T. Wu, N. Rich, S. Plunkett, L. Simpson, C. D. Fry, and K. Schenk (2014), Global simulation of extremely fast coronal mass ejection on 23 July 2012, *J. Atmos. Sol. Terr. Phys.*, **121**, 32–41, doi:10.1016/j.jastp.2014.09.013.
- Lugaz, N., and I. I. Roussev (2011), Numerical modeling of interplanetary coronal mass ejections and comparison with heliospheric images, *J. Atmos. Sol. Terr. Phys.*, **73**(10), 1187–1200, doi:10.1016/j.jastp.2010.08.016.
- Manchester, W. B., T. I. Gombosi, I. Roussev, A. Ridley, D. D. Zeeuw, I. V. Sokolov, K. G. Powell, and G. Toth (2004), Modeling a space weather event from the Sun to the Earth: CME generation and interplanetary propagation, *J. Geophys. Res.*, **109**, A02107, doi:10.1029/2003JA010150.
- Odstrcil, D., V. J. Pizzo, and C. N. Arge (2005), Propagation of the 12 May 1997 interplanetary coronal mass ejection in evolving solar wind structures, *J. Geophys. Res.*, **110**, A02106, doi:10.1029/2004JA010745.
- Pesnell, W., B. J. Dean, and P. C. Thompson (2012), Chamberlin, the Solar Dynamics Observatory (SDO), *Sol. Phys.*, **275**, 3–15.
- Reames, D. V. (1999), Particle acceleration at the Sun and in the heliosphere, *Space Sci. Rev.*, **90**(3/4), 413–491, doi:10.1023/A:1005105831781.
- Ruffolo, D. (1995), Effect of radiative deceleration on the focused transport of solar cosmic rays, *Astrophys. J.*, **442**, 861–874.
- Ruzmaikin, A., G. Li, G. Zank, J. Feynman, and I. Jun (2005), The Radial Dependence of solar Energetic Particle fluxes, in *Proceedings of Solar Wind 11 / SOHO 16, "Connecting Sun and Heliosphere" Conference (ESA SP-592)*, edited by B. Fleck, T. H. Zurbuchen, and H. Lacoste, p. 441, Whistler, Canada, 12–17 June.
- Shea, M. S., D. F. Smart, J. H. Adams, Jr., D. Chenette, J. Feynman, D. C. Hamilton, G. R. Henchman, A. Konradi, M. A. Lee, and D. S. Nachtwey (1988), Toward a descriptive model of solar particles in the heliosphere, in *Jet Propulsion Lab., California Inst. of Tech., Interplanetary Particle Environment. Proceedings of a Conference (SEE N89-28454 22-90)*, pp. 3–13.
- Shen, F., X. S. Feng, S. T. Wu, C. Q. Xiang, and W. B. Song (2011), Three-dimensional MHD simulation of the evolution of the April 2000 CME event and its induced shocks using a magnetized plasma blob model, *J. Geophys. Res.*, **116**, A04102, doi:10.1029/2010JA015809.
- Stone, E. C., et al. (1998), The solar isotope spectrometer for the advanced composition explorer, *Space Sci. Rev.*, **86**, 357–408.
- Svestka, Z., L. Fritzova-Svestkova, and J. T. Nolte (1976), Low-energy particle events associated with sector boundaries, *Sol. Phys.*, **50**, 491–500.
- Van Nes, P., R. Reinhard, T. R. Sanderson, and K.-P. Wenzel (1984), The energy spectrum of 35- to 1600-KeV protons associated with interplanetary shocks, *J. Geophys. Res.*, **89**, 2122–2132, doi:10.1029/JA089iA04p02122.
- Vourlidis, A., B. J. Lynch, R. A. Howard, and Y. Li (2013), How many CMEs have flux ropes? Deciphering the signatures of shocks, flux ropes, and prominences in coronagraph observations of CMEs, *Sol. Phys.*, **284**, 179–201, doi:10.1007/s11207-012-0084-8.
- Wang, Y., B. Wang, C. Shen, F. Shen, and N. Lugaz (2014), Deflected propagation of a coronal mass ejection from the corona to interplanetary space, *J. Geophys. Res. Space Physics*, **119**, 5117–5132, doi:10.1002/2013JA019537.
- Wang, Y.-M., and N. R. Sheeley Jr. (1990), Latitudinal distribution of solar wind speed from magnetic observations of the Sun, *Nature*, **347**, 439–444.
- Wild, J. P., S. F. Smerd, and A. A. Weiss (1963), Solar Bursts, *Annu. Rev. Astron. Astrophys.*, **1**, 291, doi:10.1146/annurev.aa.01.090163.001451.
- Wood, B. E., C.-C. Wu, R. A. Howard, D. G. Socker, and A. P. Rouillard (2011), Empirical reconstruction and numerical modeling of the first geoeffective coronal mass ejection of solar cycle 24, *Astrophys. J.*, **729**, 70, doi:10.1088/0004-637X/729/1/70.
- Wood, B. E., C.-C. Wu, A. P. Rouillard, R. A. Howard, and D. G. Socker (2012), A coronal holes's effects on CME shock morphology in the inner heliosphere, *Astrophys. J.*, **755**, 43, doi:10.1088/0004-637X/755/1/43.
- Wu, C.-C. (2009), Generation and evolution of interplanetary shocks, in *Shock Waves in Space and Astrophysical Environments: 18th Annual International Astrophysics Conference. AIP Conference Proceeding*, vol. 1183, pp. 178–186, doi:10.1063/1.3266774.
- Wu, C.-C., J. K. Chao, S. T. Wu, and M. Dryer (1996), Numerical simulation of interplanetary slow shocks in the solar wind, *Sol. Phys.*, **165**, 377–393.
- Wu, C.-C., S. T. Wu, and M. Dryer (2004), Evolution of fast and slow shock interactions in the inner heliosphere, *Sol. Phys.*, **223**, 259–282.
- Wu, C.-C., X. S. Feng, S. T. Wu, M. Dryer, and C. D. Fry (2006), Effects of the interaction and evolution of interplanetary shocks on "background" solar wind speeds, *J. Geophys. Res.*, **111**, A12104, doi:10.1029/2006JA011615.
- Wu, C.-C., C. D. Fry, S. T. Wu, M. Dryer, and K. Liou (2007a), Three-dimensional global simulation of ICME propagation from the Sun to the heliosphere: 12 May 1997 solar event, *J. Geophys. Res.*, **112**, A09104, doi:10.1029/2006JA012211.
- Wu, C.-C., C. D. Fry, S. T. Wu, M. Dryer, B. Thompson, K. Liou, and X. S. Feng (2007b), Three-dimensional global simulation of multiple ICMEs' interaction and propagation from the Sun to the heliosphere following the 25–28 October 2003 solar events, coronal mass ejections, *Adv. Space Rev.*, **40**, 1827–1834, doi:10.1016/j.asr.2007.06.025.
- Wu, C.-C., M. Dryer, S. T. Wu, B. Wood, C. D. Fry, K. Liou, and P. Simon (2011), Global Three-dimensional simulation of the interplanetary evolution of the observed geoeffective CME during the epoch August 1–4, 2010, *J. Geophys. Res.*, **116**, A12103, doi:10.1029/2011JA016947.

- Wu, C.-C., S. T. Wu, K. Liou, and S. Plunkett (2012), Evolution of a magnetohydrodynamic coronal shock, in *SPACE WEATHER: THE SPACE RADIATION ENVIRONMENT: 11th Annual International Astrophysics Conference, 19–23 March, AIP Conf. Proc.*, vol. 1500, pp. 50–55, AIP, Melville, N. Y., doi:10.1063/1.4768744.
- Xie, H., D. Odstrcil, L. Mays, O. C. S. Cyr, N. Gopalswamy, and H. Cremades (2012), Understanding shock dynamics in the inner heliosphere with modeling and Type II radio data: The 2010-04-03 event, *J. Geophys. Res.*, *117*, A04105, doi:10.1029/2011JA017304.
- Zeldovich, M. A., and B. M. Kuzhevskij (1981), Low-energy particles in interplanetary magnetic field near the sectorial boundary on September 26, 1977, in *International Cosmic Ray Conference, 17th, Paris, France, July 13–25, 1981, Conference Papers*, vol. 3, pp. 113–116, Commissariat a l'Energie Atomique, Gif-sur-Yvette, Essonne, France.
- Zhang, M., G. Qin, and H. Rassoul (2009), Propagation of solar energetic particles in three-dimensional interplanetary magnetic fields, *Astrophys. J.*, *692*, 109–132.
- Zhao, X. H., X. S. Feng, and C.-C. Wu (2007), Influence of solar flare's location and heliospheric current sheet on the associated shock's arrival at Earth, *J. Geophys. Res.*, *112*, A06107, doi:10.1029/2006JA012205.